PHYSICAL REVIEW D **89,** 044011 (2014)

Gravitational wave signatures from low-mode spiral instabilities in rapidly rotating supernova cores

Takami Kuroda,[1,2] Tomoya Takiwaki,[3] and Kei Kotake[4,1]

[1]*Division of Theoretical Astronomy, National Astronomical Observatory of Japan,*
2-21-1, Osawa, Mitaka, Tokyo 181-8588, Japan
[2]*Department of Physics, University of Basel, Klingelbergstrasse 82, 4056 Basel, Switzerland*
[3]*Center for Computational Astrophysics, National Astronomical Observatory of Japan,*
2-21-1, Osawa, Mitaka, Tokyo 181-8588, Japan
[4]*Department of Applied Physics, Fukuoka University, 8-19-1, Jonan, Nanakuma,*
Fukuoka 814-0180, Japan

(Received 16 April 2013; revised manuscript received 26 December 2013; published 11 February 2014)

We study properties of gravitational waves (GWs) from the rotating core collapse of a $15M_\odot$ star by performing three-dimensional general-relativistic hydrodynamic simulations with an approximate neutrino transport. By parametrically changing the precollapse angular momentum, we focus on the effects of rotation on the GW signatures in the early postbounce evolution. Regarding three-flavor neutrino transport, we solve the energy-averaged set of radiation energy and momentum based on the Thorne's momentum formalism. In addition to the gravitational quadrupole radiation from matter motions, we take into account GWs from anisotropic neutrino emission. With these computations, our results present supporting evidence for the previous anticipation that nonaxisymmetric instabilities play an essential role in determining the postbounce GW signatures. During prompt convection, we find that the waveforms show narrow-band and highly quasiperiodic signals which persist until the end of simulations. We point out that such features reflect the growth of the one-armed spiral modes. The typical frequency of the quasiperiodic waveforms can be well explained by the propagating acoustic waves between the stalled shock and the rotating proto-neutron star surface, which suggests the appearance of the standing-accretion-shock instability. Although the GW signals exhibit strong variability between the two polarizations and different observer directions, they are within the detection limits of next-generation detectors such as KAGRA and Advanced LIGO, if the source with sufficient angular momentum is located in our Galaxy.

DOI: 10.1103/PhysRevD.89.044011 PACS numbers: 04.25.D-, 04.30.-w, 95.85.Sz, 97.60.Bw

I. INTRODUCTION

The seminal paper [1] on the gravitational-wave emission from stellar core collapse started with the following two sentences: "The current and near-future efforts (Weiss, 1979; Epstein, 1979; Weber, 1979; Douglass and Braginsky, 1979)[2–5] to detect gravitational waves have increased the demand for reliable theoretical calculations of gravitational radiation from all possible energetic astrophysical sources. Among all potential sources, supernovae, possessing highly asymmetric cores and being situated in our own galaxy, have been thought to be the most promising candidates, probably already within the realm of second generation gravitational wave detectors."

It may be surprising that by just updating the references in the late 1970 s to the most recent ones (e.g., Advanced LIGO/VIRGO [6,7] and KAGRA [8] for an observational side), the above statements remain timeless and true,[1] outlining the final goal toward which all the relevant studies regarding the gravitational-wave (GW) signatures of core-collapse supernovae (CCSNe) have been heading since then (see recent reviews in [9,10]).

Following [1], most of the theoretical predictions have focused on the GW signals from rotational collapse of the supernova cores (e.g., [11–24] and references therein). In this context, rapid rotation of the precollapse core leads to significant rotational flattening of the collapsing and bouncing core, leading to a time-dependent quadrupole (or higher) GW emission. The steady improvement in the supernova models (e.g., the inclusion of a micro-physical equation of state (EOS), general relativity (GR), treatment of neutrino physics) recently led to a theoretically best-studied, generic, so-called type I waveform of the bounce signals. The waveform is characterized by a a sharp negative spike at bounce followed by a subsequent ring-down phase [17,18,20].

After core bounce, anisotropic matter motions due to convection [25–28] and the standing-accretion-shock-instability (SASI, [29–33]), and anisotropy in neutrino emission [28,31,34,35] are expected to be primary GW sources (see [9,10] for more details). In general, these postbounce GW signals should be more difficult to detect compared to the bounce signals, since they change much

---

[1] Although the most promising source for the first detection may likely be for compact binary mergers.

more stochastically with time as a result of chaotically growing convection and the SASI in the nonlinear hydrodynamics ([28,29,31,33,36]). However, an encouraging finding was recently reported by [35] who made a detailed analysis on the GW signals from exploding two-dimensional models with a currently best-available neutrino transport scheme. They pointed out that an episode of convective activities in the vicinity of the proto-neutron star (PNS) [33] that trigger the onset of explosion is encoded in the GW spectrogram, which could be read out by a power-excess method [37]. A combined analysis of the emergent neutrino signals [38] should provide an important clue to the supernova engine in the context of the neutrino-heating mechanism (e.g., [39–41]), which is otherwise very hard to access for conventional astronomy by electromagnetic waves (e.g., [42]).

Regarding the bounce signals,[2] rapid rotation is necessary for producing distinct GW bursts and it is likely to obtain $\sim$1% of massive star population (e.g., [43]). Minor as they may be, a high angular momentum of the precollapse core is essential for the working of the magnetohydrodynamic (MHD) mechanism [44–49]. This is because the MHD mechanism relies on the extraction of rotational free energy of the collapsing core by means of the field-wrapping and magnetorotational instability (e.g., [50–52] and references therein). It is worthwhile mentioning that such energetic MHD explosions are receiving great attention as a possible relevance to magnetars and collapsars (e.g., [53–56]), which are presumably linked to the formation of long-duration gamma-ray bursts (e.g., [57] for a review). The gravitational waveforms from the MHD explosions were found to have a quasimonotonically increasing component that is produced by the bipolar outflows [49,58,59]. Such characteristic waveforms with slower temporal evolution ($\lesssim$100 Hz) are likely to be detectable by future space-based detectors like DECIGO [60], which are free from seismic noises at the lower frequency bands.

Reliable modeling of rotating core collapse and the associated bounce signals should be done at least in three dimensions, because nonaxisymmetric instabilities are expected to naturally develop in the postbounce supernova cores (e.g., [61,62] for reviews). Probably the best understood type of instability is a classical dynamical bar-mode instability with a threshold of $T/|W| \gtrsim 0.27$ [63,64]. Here $T/|W|$ represents the ratio of rotational kinetic energy to gravitational energy. In contrast to the high $T/|W|$ instability, recent work, some of which has been carried out in idealized setups and assumptions [65–69] and later also in more self-consistent three-dimensional simulations [22,23,70] including microphysical EOS and a prescribed (Liedendörfer's) deleptonization scheme [71], suggest that a differentially rotating PNS can become dynamically unstable at much lower $T/|W|$ as low as $\lesssim$0.1. Despite clear numerical evidence for their existence, the physical origin of the low-$T/|W|$ instability remains unclear. It is most probable [67,72] that the instabilities are associated with the existence of corotation points (where the pattern speed of the unstable modes matches the local angular velocity) inside the star and are thus likely to be a subclass of shear instabilities.[3] Even in the nonrotating case, it should be mentioned that the postbounce core is no longer axisymmetric because of the growth of spiral SASI modes [74–78], which is considered to be a key ingredient for explaining the origin of pulsar's spin [74].

Since the vicinity of the PNS is an important cite for the nonaxisymmetric instabilities, general relativity (GR) and accurate neutrino transport cannot be also neglected, not to mention three-dimensional effects. In fact, Scheidegger *et al.* (2010)[23] found in their three-dimensional post-Newtonian models that the GW amplitudes become 5–10 times bigger for models including deleptonization effects than those without. As is well known, the evolution and structure of the PNSs are very sensitive to the deleptonization episode via lepton/energy transport from inside (e.g., [79–81]). In the above case, the deleptonization in the PNS results in the more compact and asymmetric core, leading to the stronger GW emission. A deeper gravitational well in GR simulations [35,82,83] compared to the corresponding Newtonian models should affect the criteria of the low-$T/|W|$ instability.

Despite the importance, recent multidimensional models both including GR and relevant microphysics are mostly limited to two dimensions (e.g., [21,35,84]), and only a handful of three-dimensional models have been so far reported [17,38,85]. Ott *et al.* (2007) [17] performed the first full three-dimensional GR simulations employing a realistic EOS and Liedendörfer's deleptonization scheme [71]. In one of their three-dimensional models with the largest GW amplitudes [17], they reported the appearance of the low-$T/|W|$ instability after around $t_{\rm pb} \sim 20$ ms postbounce, which is characterized by the dominant azimuthal density mode of $m = 1$ [65,66]. They found that the GW emission emitted in the direction of the spin axis become significantly stronger after the onset of the nonaxisymmetric instability. One of the limitations in [17] is the use of the deleptonization scheme that was originally designed to be valid only in the prebounce phase [71]. More recently, Ott *et al.* (2012) reported GR simulations employing a neutrino leakage scheme with [38] or without spatial symmetry assumptions in the computational domain [85], nevertheless, detailed analysis of the GW signals (including models with rapid rotation) has not been reported yet.

---

[2] For short, we call GW bursts emitted near bounce in the rotating iron cores the "bounce signals."

[3] Note that corotation resonance has been long known to the key ingredients in the accretion disk system, such as the Papaloizou-Pringle instability [73].

In this work, we study rotating core collapse and the bounce GW signals by performing fully general relativistic three-dimensional simulations with an approximate neutrino transport. The code is a marriage of an adaptive-mesh-refinement (AMR), conservative three-dimensional GR MHD code developed by [86], and the approximate three-flavor neutrino transport code that was developed in our previous work (see [83] for details). The spacetime treatment in the code is based on the Baumgarte-Shapiro-Shibata-Nakamura (BSSN) formalism [see, e.g., [87,88]]. Regarding neutrino transport, we solve the energy-independent set of radiation moments up to the first order and evaluate the second order momentum with an analytic variable Eddington factor (the so-called M1 closure scheme [89]). This part is based on the partial implementation of the Thorne's momentum formalism, which was extended by [90] in a more suitable manner applicable to the neutrino transport problem. By utilizing a nested grid infrastructure, an effective numerical resolution of our three-dimensional models in the center is $\Delta x \sim 450$ m, which is as good as the most recent study by [38] and is better than our previous work [83] ($\Delta x \sim 600$ m). By parametrically changing the initial angular momentum in the precollapse core of a $15M_\odot$ star [91], we follow the dynamics starting from the onset of gravitational collapse, through bounce, up to about 30–50 ms postbounce in this study. Albeit limited to the early postbounce phase (mainly due to the computational cost), we will show several interesting GW features, which come from nonaxisymmetric spiral waves that develop under the influence of the advective-acoustic cycle which is characteristic to the (spiral) SASI. Our results indicate that the low-$T/|W|$ instability might play some roles in inducing nonaxisymmetric spiral waves, although we cannot unambiguously identify the existence of the low-$T/|W|$ instability limited by our shorter simulation time ($\lesssim$30 ms postbounce) in this work.

This paper is structured as follows. In Sec. II, we briefly summarize the numerical schemes, initial models, and the method how to extract the gravitational waveforms. The main results are presented in Sec. III. We summarize our results and discuss their implications in Sec. IV.

II. NUMERICAL METHOD

This section starts with a brief summary about the basic equations and the numerical schemes of GR radiation hydrodynamics. We then move on to describe the initial conditions in Sec. II B and the method to extract the gravitational waveforms in Sec. II C, respectively.

A. GR radiation hydrodynamics

1. Metric equations

The GR radiation hydrodynamic code developed in our previous work [83] consists of the following three parts, in which the evolution equations of metric, hydrodynamics, and neutrino radiation are solved, respectively (see, [83] for more details). Each of them is solved in an operator-splitting manner, but the system evolves self-consistently as a whole satisfying the Hamiltonian and momentum constraints. Note in this section that geometrized units are used (i.e., both the speed of light and the gravitational constant are set to unity: $G = c = 1$). Greek indices run from 0 to 3, and latin indices from 1 to 3.

Regarding the metric evolution, the spatial metric γ_{ij} (in the standard $(3+1)$ form: $ds^2 = -\alpha^2 dt^2 + \gamma_{ij}(dx^i + \beta^i dt)(dx^j + \beta^j dt)$, with α and β^i being the lapse and shift, respectively) and its extrinsic curvature K_{ij} are evolved using the BSSN formulation [87,88]. The fundamental variables are

$$\phi \equiv \frac{1}{12} \ln[\det(\gamma_{ij})], \tag{1}$$

$$\tilde{\gamma}_{ij} \equiv e^{-4\phi}\gamma_{ij}, \tag{2}$$

$$K \equiv \gamma^{ij} K_{ij}, \tag{3}$$

$$\tilde{A}_{ij} \equiv e^{-4\phi}\left(K_{ij} - \frac{1}{3}\gamma_{ij}K\right), \tag{4}$$

$$\tilde{\Gamma}^i \equiv -\tilde{\gamma}^{ij}{}_{,j}. \tag{5}$$

The Einstein equation gives rise to the evolution equations for the BSSN variables as

$$(\partial_t - \mathcal{L}_\beta)\tilde{\gamma}_{ij} = -2\alpha\tilde{A}_{ij} \tag{6}$$

$$(\partial_t - \mathcal{L}_\beta)\phi = -\frac{1}{6}\alpha K \tag{7}$$

$$\begin{aligned}(\partial_t - \mathcal{L}_\beta)\tilde{A}_{ij} = {} & e^{-4\phi}[\alpha(R_{ij} - 8\pi\gamma_{i\mu}\gamma_{j\nu}T^{\mu\nu}_{(\mathrm{total})}) - D_i D_j \alpha]^{\mathrm{trf}} \\ & + \alpha(K\tilde{A}_{ij} - 2\tilde{A}_{ik}\tilde{\gamma}^{kl}\tilde{A}_{jl})\end{aligned} \tag{8}$$

$$\begin{aligned}(\partial_t - \mathcal{L}_\beta)K = {} & -\Delta\alpha + \alpha(\tilde{A}_{ij}\tilde{A}^{ij} + K^2/3) \\ & + 4\pi\alpha(n_\mu n_\nu T^{\mu\nu}_{(\mathrm{total})} + \gamma^{ij}\gamma_{i\mu}\gamma_{j\nu}T^{\mu\nu}_{(\mathrm{total})})\end{aligned} \tag{9}$$

$$\begin{aligned}(\partial_t - \beta^k\partial_k)\tilde{\Gamma}^i = {} & 16\pi\tilde{\gamma}^{ij}\gamma_{i\mu}n_\nu T^{\mu\nu}_{(\mathrm{total})} \\ & - 2\alpha\left(\frac{2}{3}\tilde{\gamma}^{ij}K_{,j} - 6\tilde{A}^{ij}\phi_{,j} - \tilde{\Gamma}^i_{jk}\tilde{A}^{jk}\right) \\ & + \tilde{\gamma}^{jk}\beta^i_{,jk} + \frac{1}{3}\tilde{\gamma}^{ij}\beta^k_{,kj} - \tilde{\Gamma}^j\beta^i_{,j} \\ & + \frac{2}{3}\tilde{\Gamma}^i\beta^j_{,j} + \beta^j\tilde{\Gamma}^i_{,j} - 2\tilde{A}^{ij}\alpha_{,j},\end{aligned} \tag{10}$$

where $\mathcal{L}_\beta$ is the Lie derivative with respect to β^i, $T^{\mu\nu}_{(\mathrm{total})}$ is the total stress-energy tensor (fluid + radiation which we shall discuss in the next subsection), D denotes covariant derivative operator associated with γ_{ij}, $\Delta = D^i D_i$,“trf” denotes the trace-free operator, and $n_\mu = (-\alpha, 0)$ is the timelike unit vector normal to the $t =$ constant time slices. Following [92], the gauge is specified by the $1 + \log$ lapse,

$$\partial_t \alpha = \beta^i \partial_i \alpha - 2\alpha K, \tag{11}$$

and by the gamma driver shift,

$$\partial_t \beta^i = k \partial_t \tilde{\Gamma}^i, \tag{12}$$

where we chose $k = 1$.

2. Radiation hydrodynamics

The total stress-energy tensor $T^{\alpha\beta}_{(\mathrm{total})}$ appeared in Eqs. (8)–(10) is expressed as

$$T^{\alpha\beta}_{(\mathrm{total})} = T^{\alpha\beta}_{(\mathrm{fluid})} + \sum_{\nu \in \nu_e, \bar{\nu}_e, \nu_x} T^{\alpha\beta}_{(\nu)}, \tag{13}$$

where $T^{\alpha\beta}_{(\mathrm{fluid})}$ and $T^{\alpha\beta}_{(\nu)}$ is the stress-energy tensor of fluid and neutrino radiation field, respectively. Note in the above equation, summation is taken for all species of neutrinos $(\nu_e, \bar{\nu}_e, \nu_x)$ with ν_x representing heavy-lepton neutrinos (i.e., ν_μ, ν_τ and their antiparticles).

Starting from the definition of $T^{\alpha\beta}_{(\nu)}$,

$$T_{(\nu)}{}^{\alpha\beta} \equiv E_{(\nu)} n^\alpha n^\beta + F^\alpha_{(\nu)} n^\beta + F^\beta_{(\nu)} n^\alpha + P^{\alpha\beta}_{(\nu)}, \tag{14}$$

the evolution equations of radiation energy $(E_{(\nu)})$ and radiation flux $(F^\alpha_{(\nu)})$ in the truncated momentum formalism [93] can be expressed as [90]

$$\begin{aligned} &\partial_t (e^{6\phi} E_{(\nu)}) + \partial_i [e^{6\phi} (\alpha F^i_{(\nu)} - \beta^i E_{(\nu)})] \\ &\quad = e^{6\phi} (\alpha P^{ij} K_{ij} - F^i_{(\nu)} \partial_i \alpha - \alpha Q^\mu n_\mu), \end{aligned} \tag{15}$$

and

$$\begin{aligned} &\partial_t (e^{6\phi} F_{(\nu)}{}_i) + \partial_j [e^{6\phi} (\alpha P_{(\nu)}{}^j_i - \beta^j F_{(\nu)}{}_i)] \\ &\quad = e^{6\phi} [-E_{(\nu)} \partial_i \alpha + F_{(\nu)}{}_j \partial_i \beta^j + (\alpha/2) P^{jk}_{(\nu)} \partial_i \gamma_{jk} + \alpha Q^\mu \gamma_{i\mu}], \end{aligned} \tag{16}$$

where Q^μ denotes the source terms. In order to simplify the neutrino-matter interactions, a methodology of neutrino leakage scheme is partly employed at this moment (see [83] for the explicit expressions).

By adopting the M1 closure [89], the radiation pressure is expressed as

$$P_{(\nu)}{}^{ij} = \frac{3\chi - 1}{2} P^{ij}_{\mathrm{thin}} + \frac{3(1 - \chi)}{2} P^{ij}_{\mathrm{thick}}, \tag{17}$$

where χ represents the variable Eddington factor, P^{ij}_{thin} and P^{ij}_{thick} correspond to the radiation pressure in the optically thin and thick limit, respectively. They are written in terms of E_ν and $F_{\nu,i}$ [90]. For the variable Eddington factor χ, we employ the one proposed by [89],

$$\chi = \frac{3 + 4\bar{F}^2}{5 + 2\sqrt{4 - 3\bar{F}^2}}, \tag{18}$$

$$\bar{F}^2 \equiv \frac{F^i F_i}{E^2}. \tag{19}$$

The hydrodynamic equations are written in a conservative form as

$$\partial_t \rho_* + \partial_i (\rho_* v^i) = 0, \tag{20}$$

$$\begin{aligned} &\partial_t \hat{S}_i + \partial_j (\hat{S}_i v^j + \alpha e^{6\phi} P \delta^j_i) \\ &\quad = -\hat{S}_0 \partial_i \alpha + \hat{S}_k \partial_i \beta^k + 2\alpha e^{6\phi} S^k_k \partial_i \phi \\ &\qquad - \alpha e^{2\phi} (S_{jk} - P\gamma_{jk}) \partial_i \tilde{\gamma}^{jk}/2 - e^{6\phi} \alpha Q^\mu \gamma_{i\mu}, \end{aligned} \tag{21}$$

$$\partial_t \hat{\tau} + \partial_i (\hat{S}_0 v^i + e^{6\phi} P (v^i + \beta^i) - \rho_* v^i) = \tag{22}$$

$$\alpha e^{6\phi} K S^k_k/3 + \alpha e^{2\phi} (S_{ij} - P\gamma_{ij}) \tilde{A^{ij}} - \hat{S}_i D^i \alpha + e^{6\phi} \alpha Q^\mu n_\mu, \tag{23}$$

$$\partial_t (\rho_* Y_e) + \partial_i (\rho_* Y_e v^i) = \rho_* \Gamma_e, \tag{24}$$

where $\hat{X} \equiv e^{6\phi} X$, $\rho_* \equiv \rho W e^{6\phi}$, $S_i \equiv \rho h W u_i$, and $S_0 \equiv \rho h W^2 - P$. ρ is the rest mass density, u_μ is the four-velocity of fluid, $h \equiv 1 + \varepsilon + P/\rho$ is the specific enthalpy, $v^i = u^i/u^t$, $\hat{\tau} = \hat{S}_0 - \rho_*$, Y_e is the electron fraction, and ε and P are the internal energy and pressure, respectively. We employ the Shen EOS [94] for baryonic matter which is based on the relativistic mean field theory (see [83] for more details on the EOS implementation).

B. Initial models

We employ a widely used progenitor of a $15 M_\odot$ star ([91], model “s15s7b2”) and impose precollapse rotation manually to study its effect during the collapse, bounce, and the early postbounce phases in a controlled fashion. We assume a cylindrical rotation profile,

$$u^t u_\phi = \varpi_0{}^2 (\Omega_0 - \Omega), \tag{25}$$

where $u_\phi = \sqrt{u_x^2 + u_y^2}$ is rotational velocity and ϖ_0 set here to be 10^8 cm is reconciled with results from stellar evolution calculations suggesting uniform rotation in the precollapse core. The initial angular velocity at the origin Ω_0 is treated as a free parameter and we compute four

TABLE I. Model summary. The second column represents the initial central angular velocity ($\Omega_{\rm ini}$) followed by $\rho_{\max,b}$ (the third column) and $\beta_{\rm b}$ (the fourth column), which represents the maximum rest mass density and rotational β parameter at bounce, respectively.

Model	$\Omega_{\rm ini}\,({\rm rad\,s^{-1}})$	$\rho_{\max,b}(10^{14}\ {\rm g\,cm^{-3}})$	$\beta_{\rm b}$
R0	0	3.54	2.3×10^{-5}
R1	$\pi/6$	3.52	1.5×10^{-3}
R2	$\pi/2$	3.41	1.3×10^{-2}
R3	π	3.28	4.9×10^{-2}

models by varying $\Omega_0 = 0,\ \pi/6,\ \pi/2$ and $\pi\,({\rm rad\,s^{-1}})$. We enumerate models as Rn, where n ranges from 0 (nonrotating) to 3 (rapidly rotating), which corresponds to the four choices of the precollapse central velocity (see Table I). Bearing in mind that it is very hard to go beyond one-dimensional computations in stellar evolution calculations and their outcomes may not be the final answer, the central angular velocity for a $15M_\odot$ star is predicted to range from 0.15 [95] to 3 (rad/s) [96], depending on whether the (prescribed) angular momentum transport is included or not [97]. The central angular velocity for models R1 and R3 is adjusted to be closely in the same range with the progenitor models (e.g., Table I). We add a random 1% initial density perturbation for all the models. By doing so, we hope to see convective activities shortly after bounce in our three-dimensional GR simulations including neutrino transport (albeit approximate) that are currently able to follow at most ~50 ms postbounce for each model (limited by the currently available supercomputing power at our hand). For model R3, we also computed two more models with different conditions as, without seed perturbation R3$_{\rm woP}$ and with switching off the neutrino-matter interaction after the bounce R3$_{\rm off}$ and one more model without seed perturbation (model $R3_{\rm delep}$), in which a deleptonization scheme [71] is employed exactly as in [17].

The outer boundary is at the radius of 7500 km and nested boxes with 9 refinement level are embedded in the computational domain without any spatial symmetry. Each box contains 128^3 cells and the minimum grid size at the origin is thus $\Delta x = 450$ m which is the same resolution with [38] and better than our previous study with $\Delta x = 600$ m [83]. In the vicinity of standing shock front $R \sim 120(240)$ km, our resolution achieves $\Delta x = 1.8(3.6)$ km which is a factor of 2(4) coarser than [38].

C. Gravitational wave extraction

From GR simulations, GWs are extractable either by gauge-dependent or -independent methods. [64] compared the waveforms emitted from oscillating neutron stars by the two methods and reported the quadrupole formula produces the waveform in a sufficient accuracy compared to the gauge-invariant method. They showed the quadrupole formula underestimates the wave amplitude by ~10%, but the phase is not changed drastically. More detailed comparison is recently reported in [98], which also supports that the quadrupole approximation is adequate for stellar collapse spacetimes with a PNS formation. Accordingly in this work we choose the conventional quadrupole formula [23,24,64,99] for extracting GWs from our simulations.

In the quadrupole formula, the transverse and the trace-free gravitational field h_{ij} is expressed by [100,101]

$$h_{ij} = \frac{A_+ e_+ + A_\times e_\times}{D}. \tag{26}$$

In Eq. (26), $A_{+/\times}$ represent amplitude of orthogonally polarized wave components, $e_{+/\times}$ denote unit polarization tensors and D is the source distance. Following [22], we adopt the same expressions for the wave amplitude $A_{+/\times}$ as

$$A_+(\theta,\phi) = \ddot{I}^{TT}_{\theta\theta} - \ddot{I}^{TT}_{\phi\phi} \tag{27}$$

$$A_\times(\theta,\phi) = 2\ddot{I}^{TT}_{\theta\phi}, \tag{28}$$

where the quadrupole moment in the spherical coordinates $\ddot{I}_{\theta\theta}$, $\ddot{I}_{\phi\phi}$, and $\ddot{I}_{\theta\phi}$ are expressed into the Cartesian components $\ddot{I}_{ij}$ as [22,102]

$$\begin{aligned}\ddot{I}^{TT}_{\theta\theta} &= (\ddot{I}^{TT}_{xx}\cos^2\phi + \ddot{I}^{TT}_{yy}\sin^2\phi + 2\ddot{I}^{TT}_{xy}\sin\phi\cos\phi)\cos^2\theta \\ &\quad + \ddot{I}^{TT}_{zz}\sin^2\theta - 2(\ddot{I}^{TT}_{xz}\cos\phi + \ddot{I}^{TT}_{yz}\sin\phi)\sin\theta\cos\theta,\end{aligned} \tag{29}$$

$$\ddot{I}^{TT}_{\phi\phi} = \ddot{I}^{TT}_{xx}\sin^2\phi + \ddot{I}^{TT}_{yy}\cos^2\phi - \ddot{I}^{TT}_{xy}\sin 2\phi, \tag{30}$$

$$\begin{aligned}\ddot{I}^{TT}_{\theta\phi} &= (\ddot{I}^{TT}_{yy} - \ddot{I}^{TT}_{xx})\cos\theta\sin\phi\cos\phi \\ &\quad + \ddot{I}^{TT}_{xy}\cos\theta(\cos^2\phi - \sin^2\phi) \\ &\quad + \ddot{I}^{TT}_{xz}\sin\theta\sin\phi - \ddot{I}^{TT}_{yz}\sin\theta\cos\phi,\end{aligned} \tag{31}$$

with superscripts TT denoting projection into the transverse-traceless gauge. The quadrupole moment I_{ij} and its time derivative are given as [64]

$$I_{ij} = \frac{G}{c^4}\int \rho_* x^i x^j d^3x \tag{32}$$

and

$$\dot{I}_{ij} = \frac{G}{c^4}\int \rho_*(v^i x^j + x^i v^j) d^3x. \tag{33}$$

The second time derivative $\ddot{I}_{ij}$ is directly computed by taking the time derivative of Eq. (33) numerically.

According to [26,36], we estimate GWs from anisotropic neutrino radiation $A^{\nu}_{+/\times}$ as

$$A^{\nu}_{+}(\xi,t) = \frac{2G}{c^4}\int_0^t dt' \int d\Omega' (1 + s(\theta')c(\phi')s(\xi) + c(\theta')c(\xi)) \times \frac{[s(\theta')c(\phi')c(\xi) - c(\theta')s(\xi)]^2 - [s(\theta')s(\phi')]^2}{[s(\theta')c(\phi')c(\xi) - c(\theta')s(\xi)]^2 + [s(\theta')s(\phi')]^2} \times R^2_{L_\nu} F^{r}_{(\nu)}{}' \tag{34}$$

and

$$A^{\nu}_{\times}(\xi,t) = \frac{2G}{c^4}\int_0^t dt' \int d\Omega' (1 + s(\theta')c(\phi')s(\xi) + c(\theta')c(\xi)) \times \frac{s(\theta')s(\phi')[s(\theta')c(\phi')c(\xi) - c(\theta')s(\xi)]}{[s(\theta')c(\phi')c(\xi) - c(\theta')s(\xi)]^2 + [s(\theta')s(\phi')]^2} \times R^2_{L_\nu} F^{r}_{(\nu)}{}'. \tag{35}$$

Here $s(A) \equiv \sin(A)$, $c(A) \equiv \cos(A)$ and $F^{r}_{(\nu)}{}'$ is radial energy flux of each neutrino species ($\nu = \nu_e, \bar{\nu}_e, \nu_x$) estimated at the radius of $(R_{L_\nu}, \theta', \phi')$. ξ denotes observer angle relative to the rotational axis and $\xi = 0$ and $\pi/2$ for polar and equatorial observers, respectively.

III. RESULTS

A. Hydrodynamic features

To summarize hydrodynamic features of our models, we first show evolution of the central (rest-mass) density and rotational β parameter (i.e., the ratio of rotational kinetic energy (T) to gravitational potential energy (W) near bounce in Fig. 1 (see also Table I in which several key quantities are summarized). Note that T and W is, respectively, defined as [103]

$$T \equiv \frac{1}{2}\int \rho_* h u_\phi v^\phi dx^3, \tag{36}$$

where $v^i = u^i/u^t$ and

$$W \equiv M_{\rm bar} - M_{\rm ADM} + E_{\rm int} + E_{\rm kin} + E_{\rm rad}, \tag{37}$$

with $M_{\rm bar}$, $M_{\rm ADM}$, $E_{\rm int}$, $E_{\rm kin}$ and $E_{\rm rad}$ being the total baryon mass, ADM mass, internal energy, kinetic energy and neutrino radiation energy, respectively.[4] The top panel of Fig. 1 shows that the central densities for all the models at bounce exceed nuclear density ($\sim 2.8 \times 10^{14}$ g cm^{-3}). As consistent with [17,38], multiple bounce does not appear also in this study, which was otherwise often observed in previous Newtonian simulations with simplified setups. From the bottom panel of Fig. 1, the β parameter at bounce reach 0.15%, 1.3%, and 4.9% for models R1, R2, and R3, which is consistent with [38] (hereafter Ott + 12). Ott + 12 reported full three-dimensional GR simulations with relatively similar schemes as ours, i.e., the BSSN formalism including neutrino leakage (but without neutrino heating). The precollapse density structure of a $12M_\odot$ star [104] employed in [38] is similar to the one employed in this work (i.e., the $15M_\odot$ star [91]). Since our model series of R0-R3 employ similar initial central angular velocity as their "s12WH07j(0-3)" in order, it is suitable to make comparisons. For instance, their β parameters for "s12WH07j(1-3)" at bounce are 0.4%, 1.6%, and 5.1%, which are in good agreement with our counterpart models (R1–R3). On the other hand, there exist some differences in numerical setups between our study and Ott + 12, including the adopted EOS, initial perturbations, and spatial restrictions. For example, the increase in the central density over the first 30 ms postbounce (e.g., Fig. 3 in [38]) is slightly milder for our models. This is because the Shen EOS employed in this work is stiffer than the Lattimer-Swesty EOS (the nuclear incompressibility $K = 220$ MeV) employed in [38]. Several important impacts on the GW emission will be mentioned later.

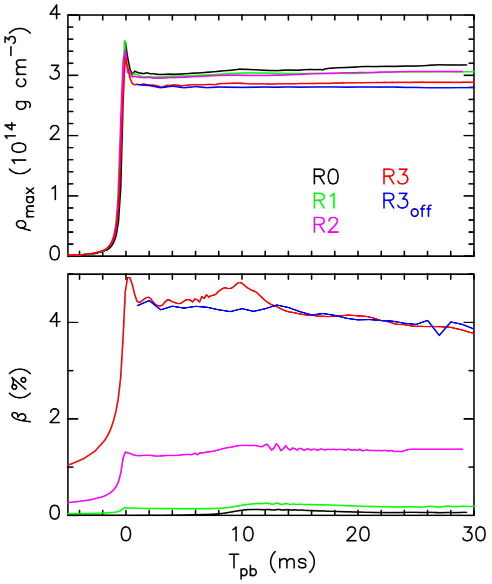

FIG. 1 (color online). Time evolution of the maximum rest mass density (top) and the rotational β parameter (bottom) as a function of postbounce time ($T_{\rm pb}$) for models R0(black line), R1 (green line), R2(magenta line), R3(red line), and R3$_{\rm off}$(blue line), respectively.

Figure 2 shows several snapshots of three-dimensional distribution of specific entropy s($k_{\rm B}$ baryon^{-1}) inside the

---

[4] Following an analogy of electromagnetic energy [103], we evaluated the contribution from neutrino radiation field, $E_{\rm rad}$, as

$$E_{\rm rad} \equiv \int T^{\alpha\beta}_{(\nu)} n_\alpha u_\beta \sqrt{\gamma} dx^3 = \int (E_{(\nu)} W - F^{i}_{(\nu)} u_i)\sqrt{\gamma} dx^3. \tag{38}$$

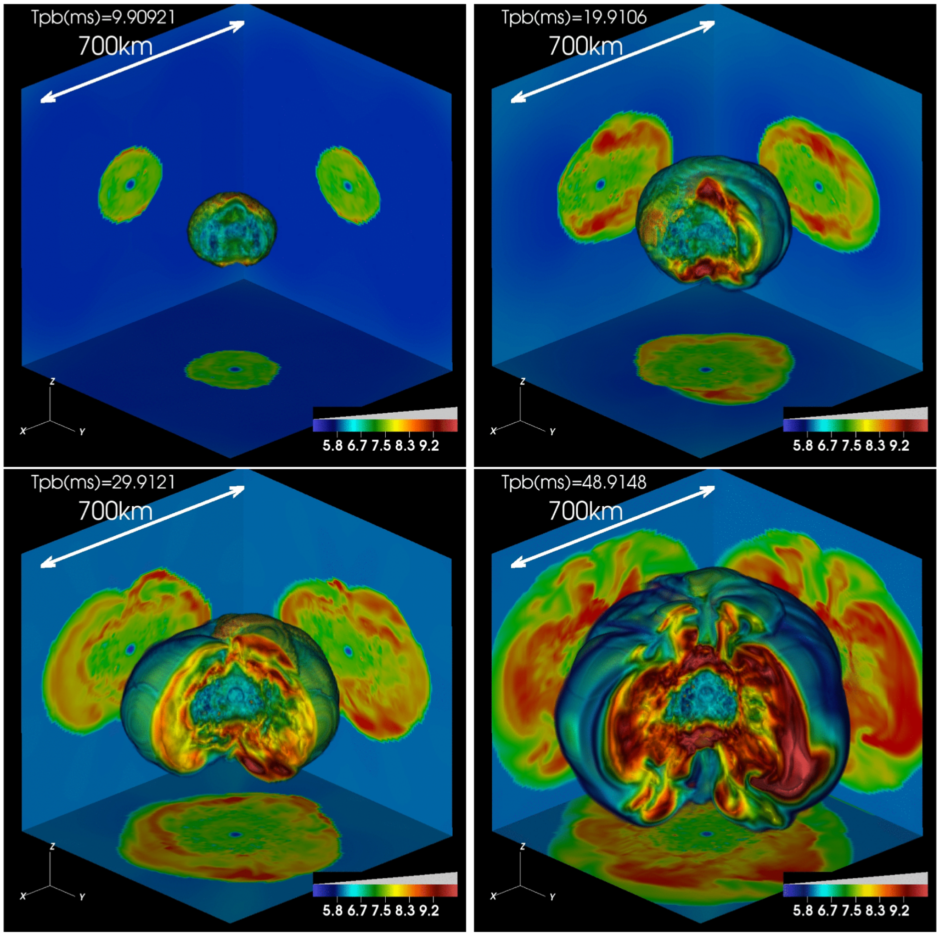

FIG. 2 (color online). Several snapshots of entropy distributions (k_B baryon^{-1}) in the central cube of 700 km^3 for model R3 (top left, $t_{pb} = 9.9$ ms; top right, $t_{pb} = 19.9$ ms; bottom left, $t_{pb} = 29.9$ ms; and bottom right, $t_{pb} = 48.9$ ms). The contours on the cross sections in the $x = 0$ (back right), $y = 0$ (back left), and $z = 0$ (bottom) planes are, respectively, projected on the sidewalls of the graphs to visualize three-dimensional structures.

central cube of 700 km^3 for model R3, the most rapidly rotating model in this study. After bounce, the shock rapidly expands in the direction toward the equatorial plane and it then stalls at an (angle-averaged) radius of ~260 km at $T_{pb} \sim 57$ ms. For the rest of models, the shapes of the shock surface remain nearly spherical (for model R0) or mildly oblate (for models R1 and R2) and the average shock radius roughly stays ~150 km within the simulation time $T_{pb} \lesssim 30$ ms (Fig. 3). These features can be also seen in Fig. 4 which shows evolution of average (dash-dotted), maximum (thick), and minimum (thin) shock radii for all the models. Pushed by strong centrifugal forces, the maximum shock extent becomes largest for the most rapidly spinning model (model R3), which is consistent with Ott + 12.

To see the effects of rotation on neutrino emission, we present in Fig. 5 the neutrino luminosities and the average neutrino energies $\varepsilon_{s_\nu,i}$. Since we do not transfer the number density of neutrinos in the present scheme (see [83] for more details), $\varepsilon_{s_\nu,i}$ can be evaluated only by the following approximate way. We first project the positions of the neutrino sphere defined in the Cartesian grids to the spherical polar grids as $R_{\nu,i}(\theta,\phi)$ for each neutrino species of $i = \nu_e, \bar{\nu}_e, \nu_x$. Then we estimate $\varepsilon_{s_\nu,i}$ by the matter temperature at the neutrino sphere assuming that neutrinos stream freely outwards with possessing the information of the last scattering surface. Accordingly ε_{s_ν} in the spherical coordinates (R,θ,ϕ) is expressed as

$$\varepsilon_{s_\nu,i}(R,\theta,\phi) \equiv \varepsilon_{\nu,i}(R_{\nu,i}(\theta,\phi),\theta,\phi). \tag{39}$$

Here $\varepsilon_{\nu,i}$ in the right-hand side denotes the neutrino energy at $R_\nu(\theta,\phi)$, which is estimated by

$$\varepsilon_{\nu,i} = k_B T \frac{F_3(\eta_\nu,0)}{F_2(\eta_\nu,0)}, \tag{40}$$

where $F_k(\eta_\nu,\beta)$ is the kth Fermi-Dirac integral, $\eta_\nu = \mu_\nu/k_B T$ is the degeneracy parameter with μ_ν and T representing the neutrino chemical potential and matter temperature, respectively, on the neutrino sphere, and β is the relativistic factor. The isotropic equivalent neutrino

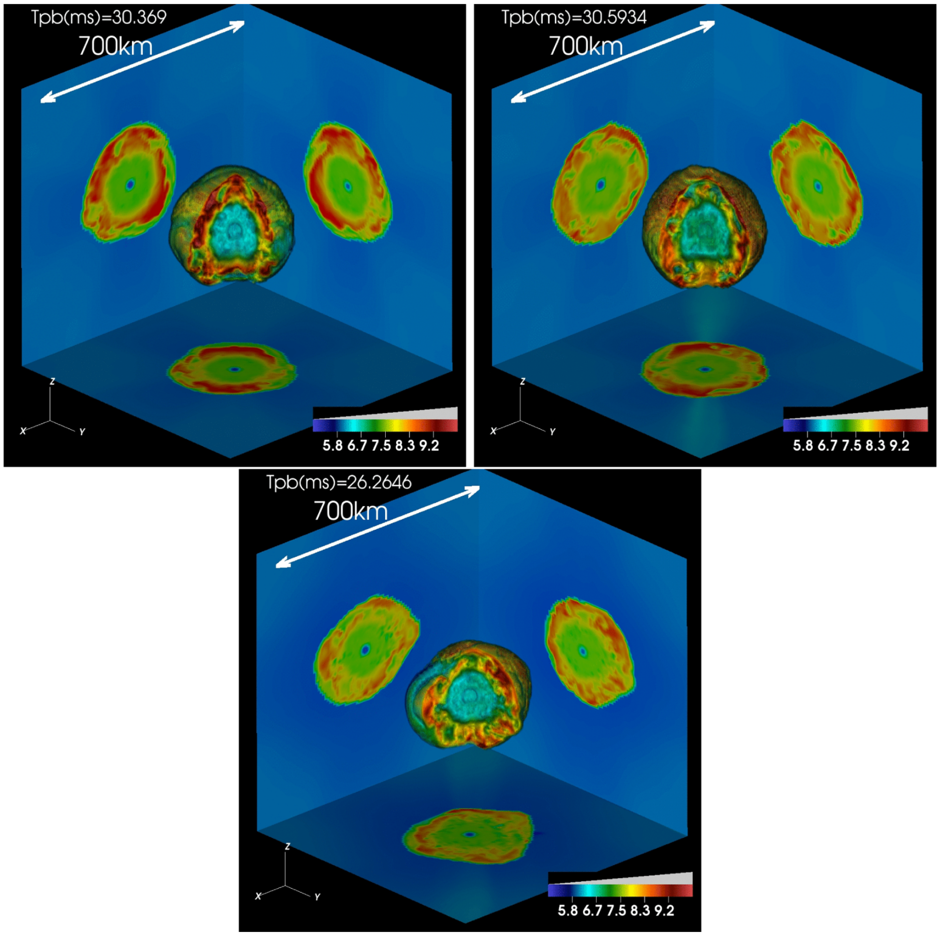

FIG. 3 (color online). Same as Fig. 2 but for the final time snapshots for models R0 (top left), R1 (top right), and R2 (bottom).

luminosity (e.g., [29]) is then evaluated by $4\pi R^2 F^r_{(\nu)}$ toward arbitrary polar angles for a given radial direction.

As is expected, the neutrino luminosity and the average neutrino energy show little observer-angle variations for the nonrotating model R0 and the peak ν_e luminosity (L_{ν_e}) reaches $\sim 3.6 \times 10^{53}$ erg s^{-1}, which is quite similar to the nonrotating model in Ott + 12. The neutrino energies of each neutrino flavor yield to the standard hierarchy (i.e., $\epsilon_{\nu_e} < \epsilon_{\bar{\nu}_e} < \epsilon_{\nu_x}$) within our simulation time. As seen from the right panels of Fig. 5, the neutrino luminosity and the average neutrino energy for model R3, on the other hand, show a clear directional dependence. The peak ν_e luminosity ($L_{\nu_e} \sim 4 \times 10^{53}$ erg s^{-1}) toward the polar direction is approximately 10% higher, compared to that along the equatorial direction (bottom right panel). By comparing with the luminosity for the nonrotating model R0 (bottom left panel), the luminosity for model R3 generally becomes higher (lower) toward the polar (equatorial) direction. Due to the competition, the total luminosity becomes slightly smaller weaker (∼6%) for model R3 compared to the nonrotating counterpart. By comparing the average neutrino energies (top left and right panels in Fig. 5), the difference between each neutrino species becomes more remarkable for model R3 (i.e., the average neutrino energy becomes higher (lower) along polar (equatorial) direction, while preserving the mentioned energy hierarchy). All of these features are predominantly because of the rotational

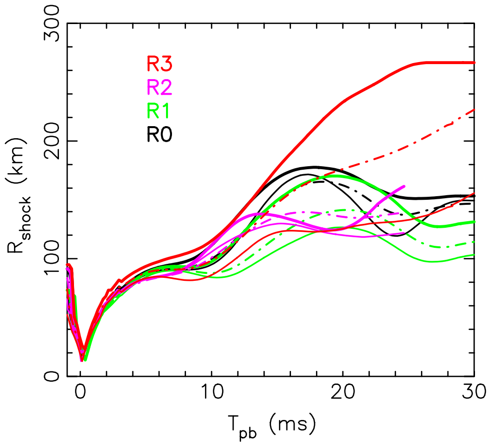

FIG. 4 (color online). Evolution of angle-average (dash-dotted), maximum (thick) and minimum (thin) shock radii as a function of postbounce time ($T_{\rm pb}$). Black, green, magenta, and red lines are for models R0, R1, R2, and R3, respectively.

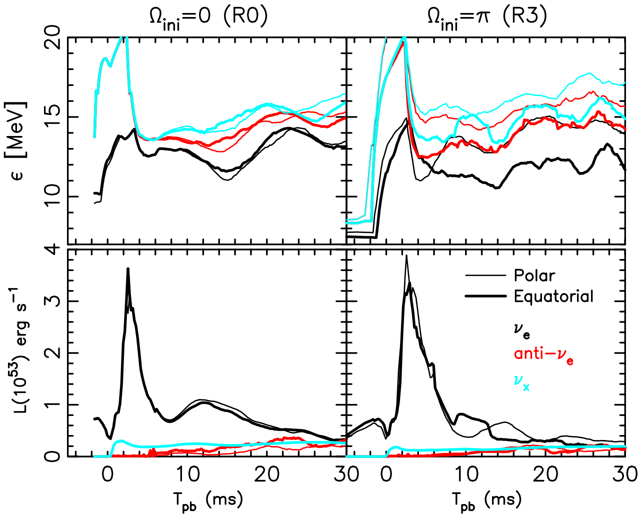

FIG. 5 (color online). Postbounce evolution of the average neutrino energies $\varepsilon_{s_\nu,i}$ (top) and the isotropic equivalent neutrino luminosities (bottom) for models R0 (left) and R3 (right). Thin and thick lines are for an observer along polar (z axis) and equatorial (x axis) directions. Black, red, and aqua lines represent electron, antielectron, and heavy-lepton neutrinos, respectively.

flattening of the core, by which the neutrino spheres of all the neutrino flavors are formed more deeper inward (outward) along the polar axis (equator), preferentially enhancing the neutrino emission along the polar direction (e.g., [105–107]). In addition, the ν_e lightcurve near at the epoch of neutronization becomes more broader for model R3, which reflects the longer dynamical timescales ($t_{\rm dyn}$) for models with larger initial angular momentum.[5] These features are in good agreement with those obtained in Ott + 12[38].

B. Gravitational-wave signatures

Now we are ready to discuss GW signatures in this section. After we shortly summarize the overall waveform trend, we perform detailed analysis on several new GW features that come genuinely from nonaxisymmetric motions from the subsequent sections.

The gravitational waveforms from matter motions for all the computed models are shown in Fig. 6.

Note in the panel that

$$A_{+/\times}\mathrm{I} \equiv A_{+/\times}(\theta = 0, \qquad \phi = 0) \tag{41}$$

and

$$A_{+/\times}\mathrm{II} \equiv A_{+/\times}(\theta = \pi/2, \qquad \phi = 0) \tag{42}$$

[e.g., Eqs. (27)–(28) and (34)–(35)] represent the quadrupole wave amplitudes with two polarizations (×, +) for equatorial (denoted as "I" in the following) and polar (as "II") directions, respectively.

From the lower left panel (for model R3's), typical GW features of the so-called type I waveforms (e.g., [19]) are clearly seen in the A_+II mode, that is, a first positive peak just before bounce precedes the deep negative signal at bounce, which is followed by the subsequent ring-down phase. The wave amplitude for model R3 is in the range of $-200 \lesssim A_+\mathrm{II} \lesssim 100$ cm near bounce. This is again comparable with that in the counterpart model "s12WH07j3" in Ott + 12. From Ott + 07 who employed the same Shen EOS (but with a more simplified treatment for deleptonization), their counterpart model (the β parameter ~6.7% at bounce) has $-240 \lesssim A_+\mathrm{II} \lesssim 90$ cm, which is also in good agreement with our model R3$_{\rm delep}$. Regarding the nonaxisymmetric GW (green lines in the right panels) in the first 10 ms postbounce, the amplitude stays negligibly small (the maximum amplitude is at most $\sim 10^{-4}$ cm), and the overall features of the waveforms during our simulation time (~30 ms postbounce) are consistent with those in Ott + 07 (their model E20 A). The wave amplitudes for our nonrotating and slow-rotating models stay much smaller ($A_+\mathrm{II} \lesssim 10$ cm) during the early postbounce evolution (models R0 (black line) and R1 (green line) in the right pair panels of Fig. 7).

By comparing model R3 (red line) with R3$_{\rm off}$ (blue line), deviation of the two waveforms becomes remarkable only after ~8 ms after bounce when the neutronization ceases. The GW amplitudes become higher for model with deleptonization (R3) compared to the counterpart model (R3$_{\rm off}$) for which deleptonization effects are turned off manually after bounce. This is also consistent with recent report by Ott + 12. As already pointed out by [23], this is because neutrino cooling in the postbounce phase leads to a more compact core (e.g., Fig. 8) with bigger enclosed mass inside, which results in a more efficient GW emission. In Fig. 8, it can be also shown that due to deleptonization, the maximum shock extent is smaller for model R3, which makes convectively unstable regions ($\mathrm{R_{ns}} \lesssim \mathrm{R} \lesssim \mathrm{R_{shock}}$) more compact than for model R3$_{\rm off}$. Then the growth time scale of prompt convection tends to be shorter which leads to strong inhomogeneity and emissions of more powerful GWs toward the spin axis together with rotation. These results confirm the previous findings (e.g., [17,23]) that accurate neutrino transport is required for a reliable GW prediction. In this respect the prediction power of our approximate neutrino transport scheme is limited, which should be tested by three-dimensional GR models with more detailed neutrino transport.

Figure 9 shows the waveforms from anisotropic neutrino emission [Eqs.(34)–(35)]. Due to the *memory effect* inherent to the neutrino GWs (e.g., [108]), the waveforms exhibit much slower temporal variation compared to the matter

---

[5] This is because the central density (ρ_c) supported by the centrifugal forces becomes smaller ($t_{\rm dyn} \propto \rho_c^{-1/2}$) for rapidly spinning models (e.g., top panel of Fig. 1).

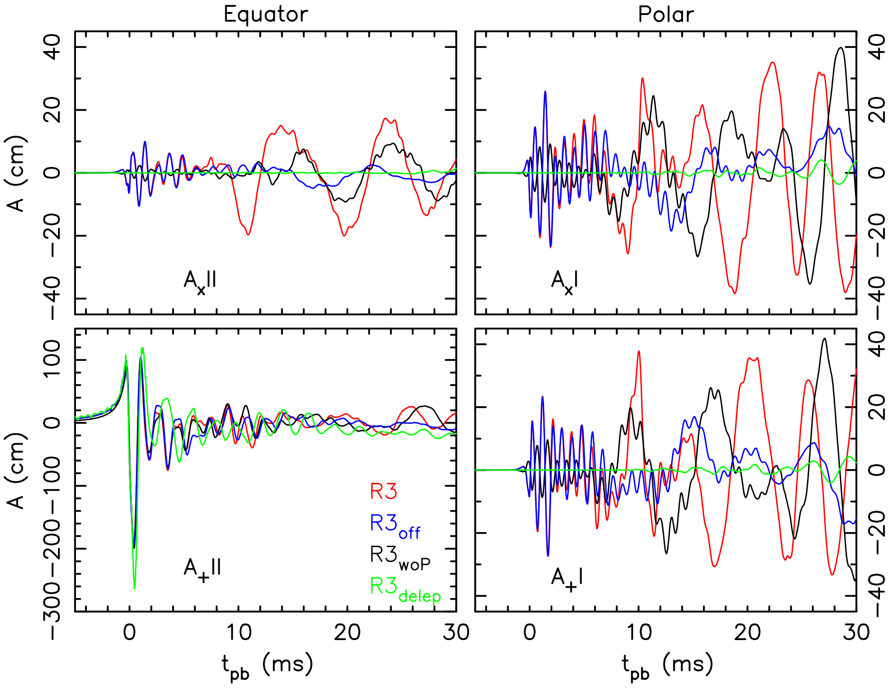

FIG. 6 (color online). Gravitational waveforms from matter motions for equatorial and polar directions (left half and right half in the pair panels, respectively) with two polarizations [top half (×) and bottom half (+)] for a series of our fastest rotating models R3 [R3 (red line), $R3_{\rm off}$ (blue line), $R3_{\rm woP}$ (black line), and $R3_{\rm delep}$ (green line)].

GWs. From the lower left panel, the largest amplitude of the neutrino GWs is obtained for the A_+II mode in model R3 (red line), which reaches ∼6 cm with a quasimonotonically increasing trend during the simulation time. This characteristic feature was already reported so far either in two-dimensional simulations employing detailed neutrino transport [28] or in three-dimensional simulations with idealized setups [36]. This comes from the (mentioned)

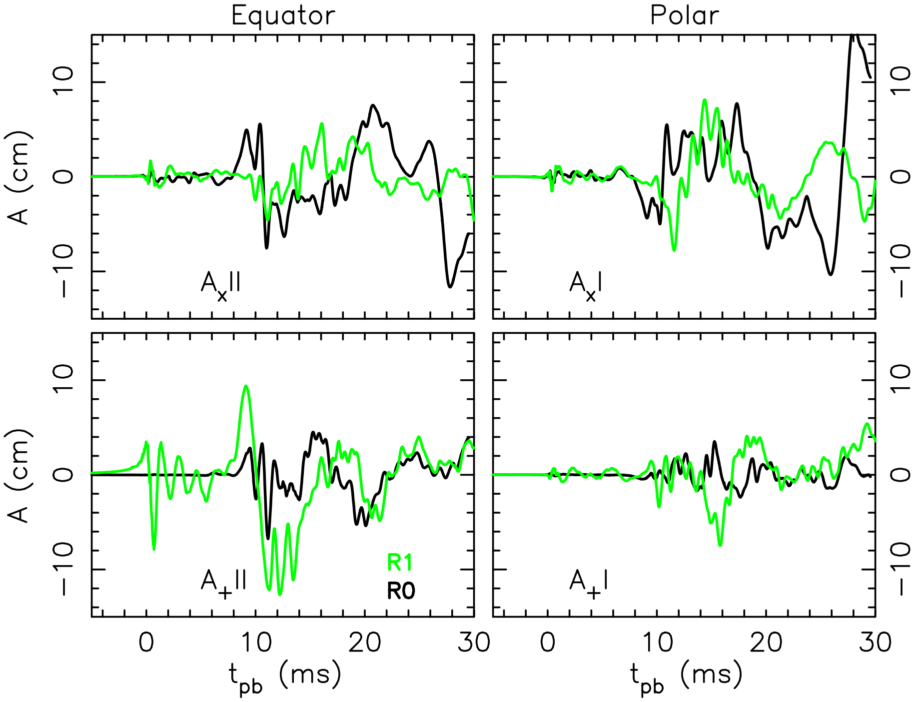

FIG. 7 (color online). Same as Fig. 6 but for models R0 (black line) and R1 (green line).

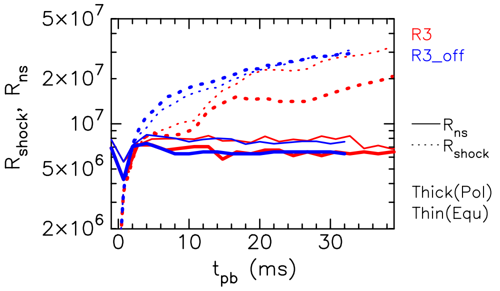

FIG. 8 (color online). Time evolution of the shock (R_{shock}, dotted line) and the PNS (R_{ns}, solid line) radii for models R3 (red line) and $R3_{off}$ (blue line), respectively. R_{ns} is defined at $\rho = 10^{11}\ \mathrm{g\,cm^{-3}}$. Thick and thin line styles represent the positions of R_{shock} and R_{ns} along the polar axis and equatorial plane, respectively.

stronger neutrino emission along the rotation axis due to the deformed neutrino sphere in the rapidly spinning cores. Except for model R3, the wave amplitudes from neutrinos stay around a few cm during our short simulation time.

C. Nonaxisymmetric imprints

Now let us have a look at again the matter GW signals for the $A_{+/\times}\mathrm{I}$ modes [emitted toward the pole, e.g., the right-half panel of Fig. 6 (left)]. Note that these signals come genuinely from nonaxisymmetric matter motions. The red lines (model R3) in these panels show an oscillating behavior with two different modulation timescales ($:\tau_{\mathrm{mod}}$), firstly in a very short timescale ($\tau_{\mathrm{mod}} \lesssim 1$ ms) promptly after bounce within $t_{\mathrm{pb}} \lesssim 8$ ms, and secondly in a relatively longer modulation ($\tau_{\mathrm{mod}} \gtrsim 10$ ms) after that. These features are only clearly visible for our rapidly rotating model R3.

For model R3, the wave amplitudes in the first epoch ($t_{\mathrm{pb}} \lesssim 8$ ms) reach $|A_{+/\times}\mathrm{I}| \sim 20$ cm, while non- and slowly rotating models (R0 and R1) meanwhile produce very little GW emission ($|A\mathrm{I}| \lesssim 1$ cm). By comparing with the luminosity curves in Fig. 5, this epoch is shown to closely correlate with the neutronization phase. During this epoch, the prompt shock propagates rapidly outward with capturing electrons and dissociating infalling iron group nuclei until the prompt shock stalls at around $t_{\mathrm{pb}} \sim 10$ ms. As seen from Fig. 4, the shape of the shock for all the models is rather spherical at this time, regardless of the difference in the initial rotation rates. In such a short duration after bounce, possible reason of producing the nonaxisymmetry is less likely to be the low-$T/|W|$ instability, not to mention the SASI.

The black and red curve in Fig. 10 corresponds to the $A_+\mathrm{I}$ and $A_\times\mathrm{I}$ mode waveform of model R3 (see also red line in Fig. 6), respectively. At the very early postbounce phase ($t_{\mathrm{pb}} \lesssim 8$ ms), the phase of the quasioscillatory pattern of the two modes (black and red curves) is shifted about $\pi/2$. Such feature of the phase-shifted pattern should be coincided with the bar mode deformation ($\ell = 2, m = 2$).[6] The (nondimensional) amplitudes of the $m = 2$ mode in Fig. 10 (pink line) supports this anticipation. Here we estimate the normalized azimuthal Fourier components A_m as

$$A_{\mathrm{m}} = \frac{\int_0^{2\pi} \rho(\varpi, \phi, z = 0) e^{i\mathrm{m}\phi} d\phi}{\int_0^{2\pi} \rho(\varpi, \varphi, z = 0) d\phi}, \tag{43}$$

where the $m = 2$ mode is evaluated at a given radius of $\varpi \equiv \sqrt{x^2 + y^2} = 20$ km. Regarding the mode amplitudes and the GW emission, the $m = 2$ mode amplitudes is $\sim 10^{-2}$ (e.g., the label of A_m in Fig. 10) at the very early postbounce phase, which results in the GW emission of ~ 20 cm. This is in good agreement with [17] (in their Fig. 3) who showed the $m = 2$ mode amplitudes of 10^{-2} leads to the wave amplitude ~ 30 cm. These results might suggest the $m = 2$ mode from the seed perturbations could dominantly act as the source of the GW emission. But it should be noted that our model $\mathrm{R3_{woP}}$ that does not have initial seed perturbations (see black line in Fig. 6) produce non-negligible GW emission at the very early postbounce phase ($\lesssim 6$ cm), although the wave amplitude is smaller than that for model R3 that has seed initial perturbations (Fig. 12)[7]

As the neutronization phase comes to an end at around $t_{\mathrm{pb}} \sim 8$ ms (Fig. 5), the prompt shock simultaneously stagnates, triggering the entropy-driven prompt convection behind. After that, the waveforms for moderately and rapidly spinning models (R2 and R3) exhibit a longer modulation with slightly larger amplitudes ($|A| \sim 20$ cm) compared to those near the neutronization phase. Non- (R0) and slowly (R1) rotating models emit roughly ~ 10 times stronger GWs. These amplitudes during prompt convection are in accord with previous studies, $|A| \sim 15$ cm in [38,85], $|A| \sim 20$ cm in [35], and $|A| \sim 8$ cm in [23].

As seen from red line in Fig. 6 (left panel), the waveform of model R3 has a clear sinusoidal modulation, which possesses a $\pi/2$ phase shift between $A_+\mathrm{I}$ and $A_\times\mathrm{I}$. This

---

[6] As is well known in the case of the GW emission from binary coalescence.

[7] The nonvanishing components could come from intrinsic numerical perturbations, which are unavoidable for any code using a Cartesian grid (see discussions in [85]). In addition, we have to add that when we employ only the Liebendoerfer's deleptonization scheme in model R3 (without neutrino leakage scheme), the wave amplitude at the very early postbounce phase becomes very small ($\sim 10^{-4}$ cm). Remembering that the leakage scheme is nothing but a very crude approximation of neutrino transport, further investigation is needed to clarify the in-depth analysis about the impacts of initial seed perturbations on the early postbounce GW signals. This should require a systematic study, in which a variety of three-dimensional GR models are to be computed with refined numerical resolutions and with more sophisticated transport scheme, which we consider as a very important extension of this study.

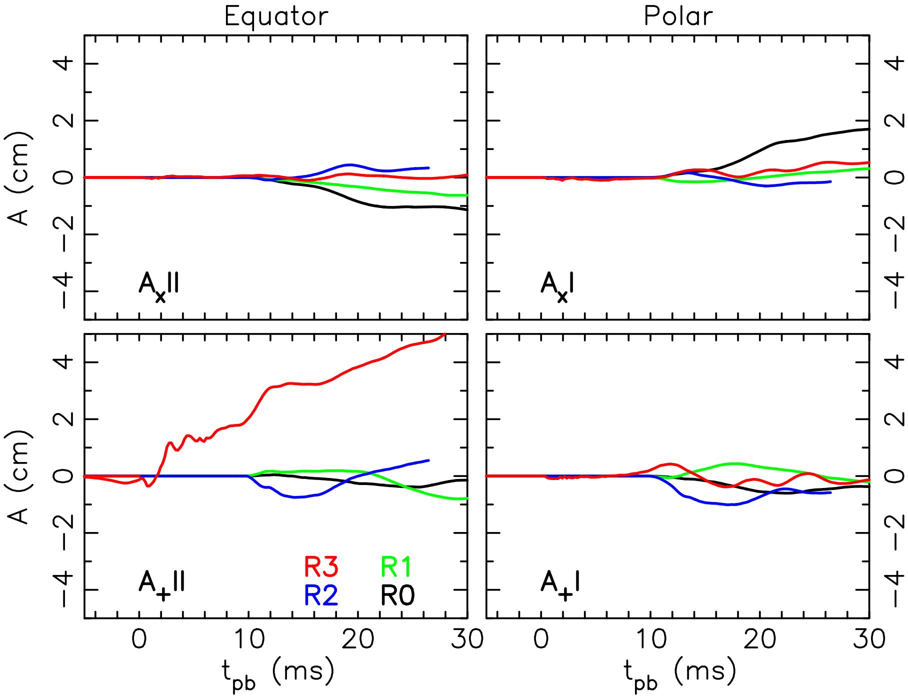

FIG. 9 (color online). Same as Fig. 6 but for the waveforms from anisotropic neutrino emission (sum of the contributions from all the neutrino species).

feature persists until the end of simulations ($t_{\mathrm{pb}} \lesssim 50$ ms in this study). To understand the origin of the sinusoidal signature, we present a spectrogram analysis in Fig. 12. In the figure, the angle-dependent characteristic strain h_{char},

$$h_{\mathrm{char}}(\theta,\phi,F) = \sqrt{\frac{2}{\pi^2}\frac{G}{c^3}\frac{1}{D^2}\frac{dE(\theta,\phi)}{dF}}, \qquad (44)$$

is plotted (e.g., [16,33,37]), where D represents the source distance that we assume as $D = 10$ kpc (unless otherwise stated), F is the GW frequency, and $dE(\theta,\phi)/dF$ is the GW spectral energy density. $dE(\theta,\phi)/dF$ is given by[8]

$$\frac{dE}{dF} = \frac{\pi}{4}\frac{c^3}{G}F^2(|\tilde{A}_+(F)|^2 + |\tilde{A}_\times(F)|^2). \qquad (45)$$

Here $\tilde{A}(F)$ denotes the Fourier component of $A(t)$ [33] that is defined as

$$\tilde{A}_{+/\times}(F) = \int_{-\infty}^{\infty} A_{+/\times}(t)H(t-\tau)e^{-2\pi iFt}dt, \qquad (46)$$

where the width of the Hann window τ is set as 10 ms.

The spectrogram for the equatorial GW (top right panel) near bounce ($t_{\mathrm{pb}} \sim 0$ ms) shows a power excess (colored by yellow to reddish regions) in the range between $100 \lesssim F \lesssim 1000$ Hz, which is associated with the best-studied type I signals (e.g., [17,18,20]).[9] Not surprisingly, this feature is hardly seen in the nonrotating model (bottom right panel in Fig. 8). Since the deviation from spherical symmetry for model R0 is very small in the early postbounce phase, little angular variations are seen in the GW spectrogram (compare bottom left with bottom right panel). On the other hand, the spectrograms for model R3

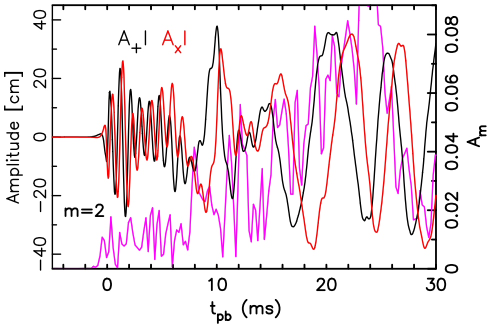

FIG. 10 (color online). Gravitational waveforms from matter motions for polar direction in model R3. Black and red lines are for A_+I and $A_\times$I, respectively. The pink curve represents non-axisymmetric mode amplitude with $m = 2$ [e.g., Eq. (43)] of matter distribution at a given radius $\varpi = 20$ km.

---

[8] The angle dependence (θ,ϕ) is omitted for the sake of brevity.

[9] In line with previous works, these type I signals are likely within the detection limits of the next generation detectors for a Galactic source, when the β parameter at bounce exceeds $\sim$1% (e.g., model R2 in this work).

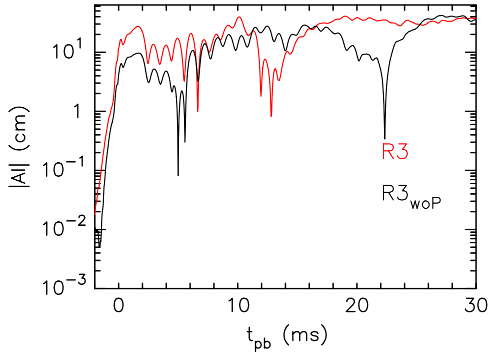

FIG. 11 (color online). The absolute GW amplitude of $|AI|$ [toward the polar direction, Eq. (42)] for our most rapidly rotating model R3 with (red line) and without (black line) initial seed perturbations.

have much clearer angular dependencies (compare top left with top right panel). The polar GW spectrogram (top left panel) has two distinct power-excess *islands* that are enclosed by black solid line (satisfying the signal-to-noise ratio: SNR $\gtrsim 1$ for a Galactic source by the second generation detectors). The typical GW frequency of the first island is about ∼1000 Hz between $0 \lesssim t_{\mathrm{pb}} \lesssim 10$ ms (a reddish zone near the top left corner in the top left panel), and it is around 200–250 Hz for the second island with its excess clearly visible from $t_{\mathrm{pb}} \gtrsim 10$ ms (e.g., a horizontal reddish stripe covering its peak around 200–250 Hz in the panel).

The first island, which is narrower (in width and height) than the second one in the frequency-time domain, originates from the initial seed perturbations that we mentioned above. It is interesting to point out that the resulting GW amplitudes satisfy SNR $\gtrsim 1$ (enclosed by black solid line) for a Galactic source. In addition to the well-studied equatorial GWs[10] (associated with the type I signals), our results suggest that the *polar* GWs just after bounce have also a unique signature, which is produced by the percent levels of the precollapse density fluctuations seeded in the rapidly rotating cores.

Regarding the second island, the characteristic frequency $F_{\mathrm{char}} = 200$–250 Hz for model R3 ($t_{\mathrm{pb}} \gtrsim 10$ ms, top left panel)[11] is higher than those ($F_{\mathrm{char}} \sim 100$ Hz) in models R0 and R1 (compare Figs. 8 and 13). Note that the lower characteristic frequency ($F_{\mathrm{char}} \sim 100$ Hz) observed in our nonrotating and only mildly rotating models is consistent with recent results by [35] who performed two-dimensional GR simulations including detailed neutrino transport. According to their analysis, the GWs during prompt convection are predominantly generated by radially propagating acoustic waves above the PNS. With the typical sound velocity there ($C_s \sim 10^9\ \mathrm{cm\,s^{-1}}$) and the shock radius ($R_{\mathrm{shock}} \sim 100$ km), the typical frequency in our three-dimensional full-GR results ($F_{\mathrm{char}} \sim C_s/R_{\mathrm{shock}} \sim 100$ Hz) can be also reasonably estimated. On the other hand, the characteristic frequency for the second island ($F_{\mathrm{char}} = 200 \sim 250$ Hz, most clearly visible for model R3, e.g., top left panel in Fig. 8) is shown to be systematically higher than the GW component solely from the propagating acoustic waves. From the next section, we look into the reason of the higher frequency in more detail. Touching on the detectability, the relevant GW frequencies (regardless of the difference) are in the range of $F_{\mathrm{char}} \sim 100 - 250$ Hz, which are close to the maximum detector sensitivity for the second generation interferometers (e.g., KAGRA and Advanced LIGO [6,8]).

D. GW emission from one-armed spiral waves

In this section, we are going to discuss that the characteristic frequency ($F_{\mathrm{char}} = 200 \sim 250$ Hz); clearly visible in the GW spectrogram for model R3 has a tight correlation with the one-armed spiral waves. We will also show that these features can be naturally explained by the acoustic feedback between the stalled shock and the rotating PNS surfaces, which is thus reconciled with the well-established picture of the SASI ([110–112]).

Similar to the right panels in Fig. 12, but we plot in Fig. 14 contributions to the first time derivative of the mass quadrupole moment [Eq. (33)] from different radial locations (seen from the polar direction). The top, middle, and bottom panels represent h_{char} evaluated by the spatial integral in the following range, within $R < 20$ km, $20 < R < 60$ km, and $R > 60$ km, respectively. It can be seen that the GW emission in the second island (again, the horizontal ($F_{\mathrm{char}} = 200 \sim 250$ Hz) reddish zone after around $T_{\mathrm{pb}} \sim 10$ ms) are radiated mainly from above the PNS ($R \gtrsim 60$ km, bottom panel) during prompt convection. Note that the spatial location itself is similar to the one reported in [35] for their nonrotating model.

To see how the source of the strong GW emitter evolves with time, Fig. 15 shows the integrand ψ in the quadrupole formula (top panel),

$$\psi \equiv (A_+ \mathrm{I})^2 + (A_\times \mathrm{I})^2 = (\ddot{I}_{xx} - \ddot{I}_{yy})^2 + (2\ddot{I}_{xy})^2, \qquad (47)$$

and the specific entropy (bottom panel) at selected time slices. From the upper panels (regarding ψ), it can be seen that the one-armed spiral wave starts to form at around [e.g., $T_{\mathrm{pb}} = 16.74$ ms, top middle panel (upper)] for model R3, and then it keeps rotating in a counterclockwise manner (compare $T_{\mathrm{pb}} = 26.75$ ms and $T_{\mathrm{pb}} = 28.75$ ms) until the end of simulations. From the two panels (at $T_{\mathrm{pb}} = 26.75$ and 28.75 ms), the spiral wave rotates around ∼90° during 2 ms, thus the rotational period (frequency) can be estimated as $T_{\mathrm{rot}} \sim 8$ ms and $2/T_{\mathrm{rot}} \sim 250$ Hz.[12] Note that

---

[10] We shortly call GWs seen from the polar (equatorial) direction as polar (equatorial) GWs, respectively.

[11] E.g., the horizontal dotted line that closely divides the island into two.

[12] Here 2 in the numerator comes from two polarized wave modes (+/×).

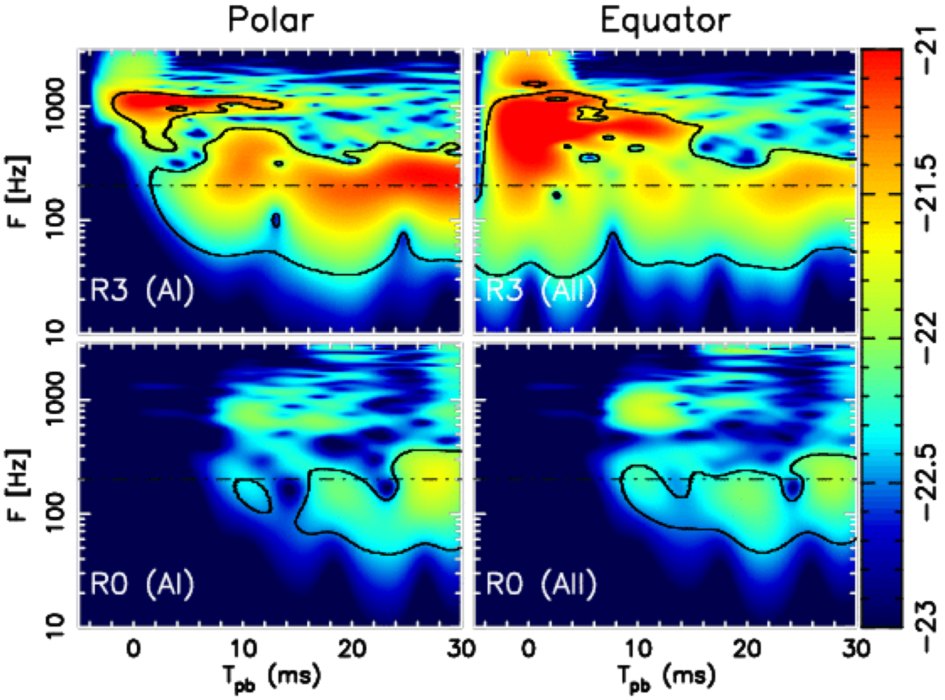

FIG. 12 (color online). Color-coded GW spectrograms [$\log_{10}(h_{\rm char})$, Eq. (44)] for models R3 (top) and R0 (bottom). Left and right panels are for polar $(\theta, \phi) = (0, 0)$ and equatorial $(\theta, \varphi) = (\pi/2, 0)$ directions, respectively. The model name with the polarized mode is given in the lower left corner of each panel (for example, "R3 (AI)" in the top left panel). The contour drawn by the black solid line in each panel corresponds to a threshold beyond which the signal-to-noise ratio (SNR) for KAGRA [109] exceeds unity (for a Galactic event). To guide the eyes (see text for details), the horizontal dotted line (200 Hz) is plotted. To clearly present the postbounce GW signatures, we set the maximum value of the color scale as $\log_{10}(h_{\rm char}) = -21$, while the wave amplitude is actually more higher near bounce ($\log_{10}(h_{\rm char}) \sim -20.3$ in the AII mode [top right panel)].

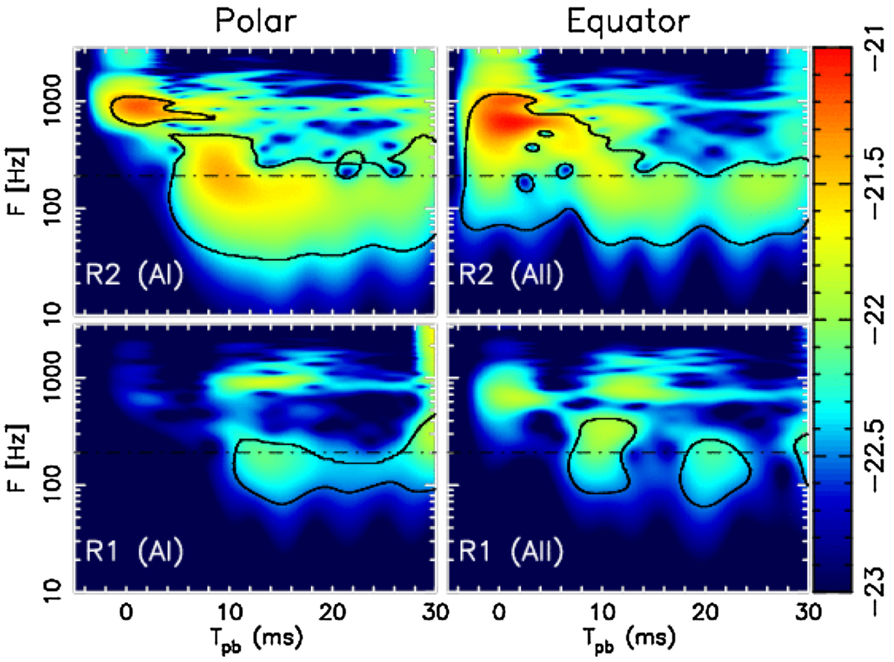

FIG. 13 (color online). Same as Fig. 12 but for models R2 (top) and R1 (bottom).

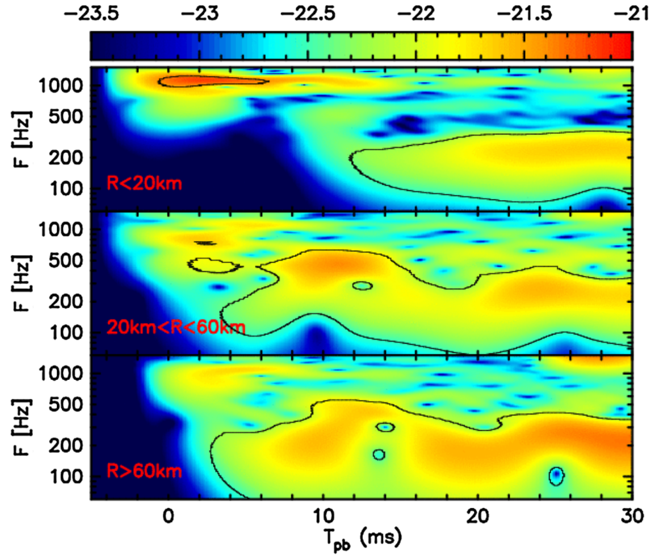

FIG. 14 (color online). Similar to the right panels of Fig. 12, but contributions to the first time derivative of the mass quadrupole moment $\dot{I}_{ij}$ are presented for different radial locations from the innermost ($R < 20$ km, top), 20 km $< R <$ 60 km (middle), to the outer region ($R > 60$ km, bottom), respectively. Note in this panel that GWs seen from polar direction are plotted.

this is close to the mentioned GW frequency $F_{\rm char} =$ 200–250 Hz (e.g., Fig. 12). Comparing with the lower panels, the spiral mode is seen to connect between the standing shock front (the reddish high-entropy regions between the outer blueish regions and inside) and the vicinity of the PNS ($\sim 50-60$ km in radius). In the next section, we are moving on to seek the possible origins of the spiral waves in more detail.

Here we shortly mention that the appearance of the spiral wave is unlikely to be seeded by nonconservation of momentum of the three-dimensional hydrodynamic simulations. To check it, we plot in Fig 16 that shows a postbounce evolution of the deviation of the mass center from the origin. The mass center (C_x, C_y, C_z) in the Cartesian coordinates is defined as,

$$C_i \equiv \frac{\int \rho_* x^i dx^3}{\int \rho_* dx^3}. \tag{48}$$

Figure 16 shows the relative displacement of the mass center estimated at a fixed radius of 20 km. The mass center does not strictly stay in the very center, and the deviation maximally reaches $\sim 2\%$ after $t_{\rm pb} \gtrsim 10$ ms, when nonaxisymmetric features are more clearly visible as shown in Fig. 15. But the deviation never grows significantly in the simulation time ($t_{\rm pb} \lesssim 30$ ms). Furthermore, since the absolute value of the displacement (20 km × 0.02–0.4 km) is (albeit slightly) smaller than the finest grid size $\Delta {\rm x} = 450$ m, C_i is located inside the innermost grid for every direction ($i = x, y, z$). We thus consider that the momentum is conserved with a resolvable accuracy. Note also that a vigorous growth of the one-armed spiral waves was observed also in the three-dimensional post-Newtonian models including a neutrino transport effect by [23] around a similar postbounce timescale with ours (see their lower middle panel of Fig. 16). Above facts indicate that nonaxisymmetric instabilities observed in our simulations do not come simply from a numerical artifact.

E. Possible origins of one-armed spiral waves

In this section, we will discuss what kind of rotational instabilities took place, triggered the one-armed spiral waves and how they affect on the GW emissions. We consider two types of rotational instability may coexist which are (1) the low-$T/|W|$ instability [17,23] which is mainly originated from the central PNS and (2) the spiral SASI [74–78] which is originated from the stalled shock. We will discuss these instabilities more deeply in followings.

In order to more clearly specify the nonaxisymmetic structures, we first monitor density profiles at a given radius $\varpi \equiv \sqrt{x^2 + y^2}$ in the equatorial plane in Fig. 17, which are evaluated by Eq. (43). For a mildly rotating model (R1, left panel of Fig. 17),@the Cartesian $m = 4$ background noise (red lines) shows relatively stronger signals than the other modes inside the PNS ($\varpi = 20$ km, thick line) and at the shock ($\varpi = 130$ km, thin line) compared to rapidly rotating model R3.

We here shortly discuss whether these nonaxisymmetric mode amplitudes within $T_{\rm pb} \lesssim 10$ ms (e.g., $A_{\rm m} \sim 10^{-2}$ for model R3) are consistent with the resulting GW amplitudes (~ 10 cm) seen in Fig. 6 along the pole. Based on an order-of-magnitude estimation, the GW amplitude (that we denote here as A) emitted from matter with mass quadrupole moment $2M^2/R$ and with a measure of nonsphericity ε can be roughly estimated as

$$A \sim \varepsilon \frac{2M^2}{R} \sim \varepsilon \cdot 10^5 \frac{M}{M_\odot} ({\rm cm}), \tag{49}$$

where M and R represents the mass and size of the system, respectively. When we measure ε from $A_{\rm m}$ and take $M \sim 0.1 M_\odot$ (typical value in the simulation time), the estimated GW amplitude becomes $\mathcal{O}(10)$ and $\mathcal{O}(10^2)$ cm for models R1 and R3, respectively. This is in good agreement with the obtained GW amplitudes, which suggests that percent levels of the nonaxisymmetric mode amplitudes lead to sizable GW emission along the pole (e.g., Fig. 6). In addition, [17] reported GW amplitudes ~10 cm with nonaxisymmetric mode amplitude $A_{\rm m} \sim 1\%$ (see, their Fig. 3) which is quantitatively consistent with our results.

On top of the Cartesian noise, the linear growth of $m = 1$ mode (inside the PNS for model R3, thick blue line) is clearly seen in the right panel, which gradually transits to

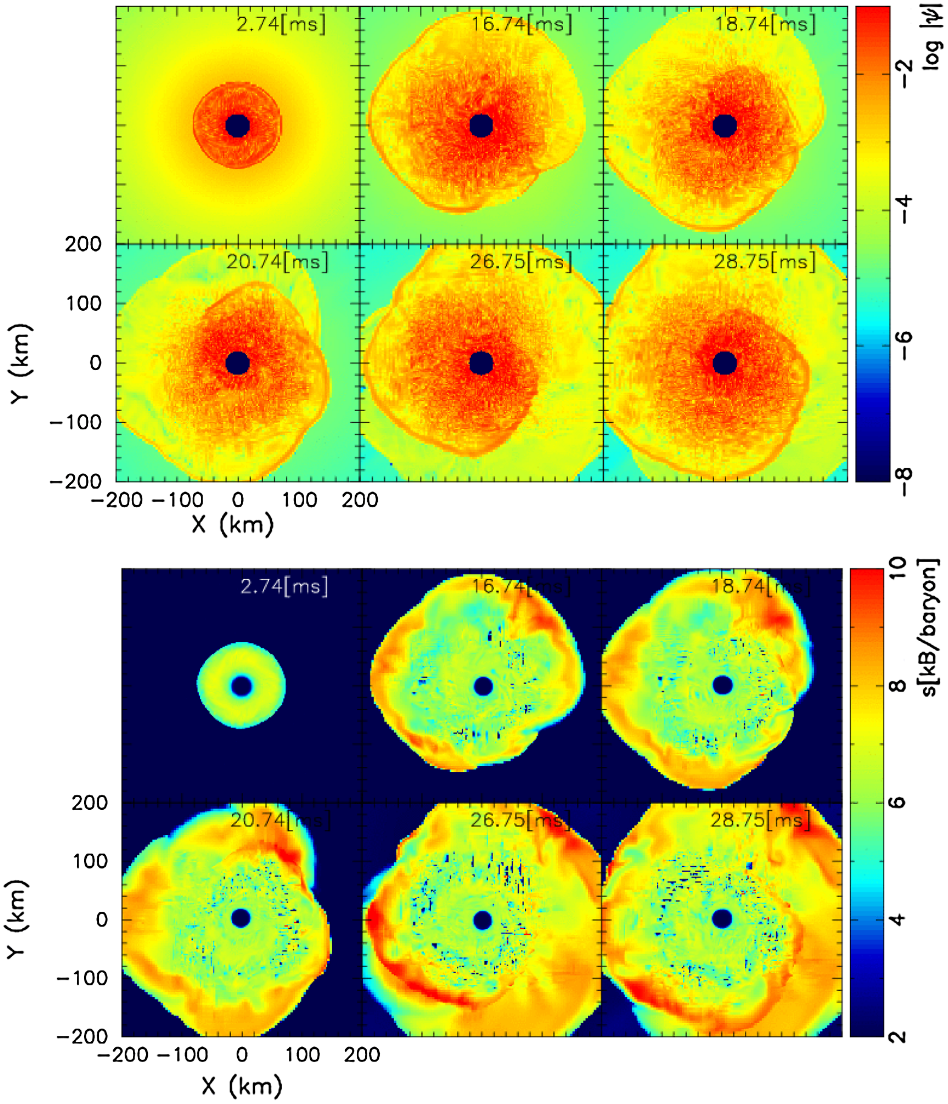

FIG. 15 (color online). Color maps of the integrand ψ in the quadrupole formula (top) and entropy (per baryon, bottom) on the equatorial plane at selected time slices (denoted in the top right corner in each mini panel) for model R3. In the upper panels plotting ψ, the central region $R \leq 20$ km is excised to show a clear contrast. Note that the color scale is in a logarithmic scale and it is normalized by the maximum value of ϕ.

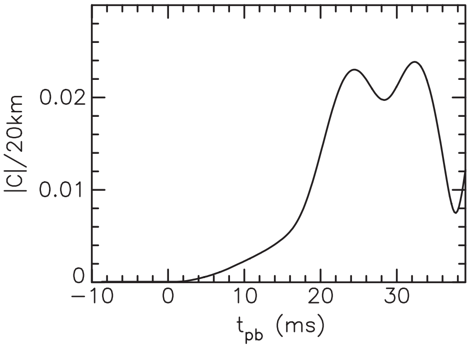

FIG. 16. Postbounce evolution of the deviation of the mass center ($|C| = \sqrt{C_x^2 + C_y^2 + C_z^2}$) in the Cartesian coordinates from the origin for model R3. The relative displacement of the mass center is estimated at a fixed radius of 20 km.

the saturation phase as the prompt convection phase sets in ($t_{\rm pb} \gtrsim 10$ ms). Note that from the thin blue line (right panel, for $\varpi = 130$ km), the presence of the one-armed spiral waves behind the shock (compare Fig. 15) is evident.

The dominant $m = 1$ mode at the surface of PNS ($\varpi = 20$ km) is considered to be of a remarkable signature of the low-$T/|W|$ instability reported by, e.g., [17,23]. Their studies showed that the frequency of the GWs associated with the instability typically peaks around ~1 kHz. As seen from the top panel of Fig. 14 (e.g., the spectrogram inside from $R \leq 20$ km at $T_{\rm pb} \sim 20$ ms), there does exist some excess near 1 kHz before our simulations terminated (30 ms postbounce). But the excess is more clearly visible around ~200 Hz, which comes from outside the PNS. It takes typically several ten milliseconds after bounce before the low-$T/|W|$ instability fully develops

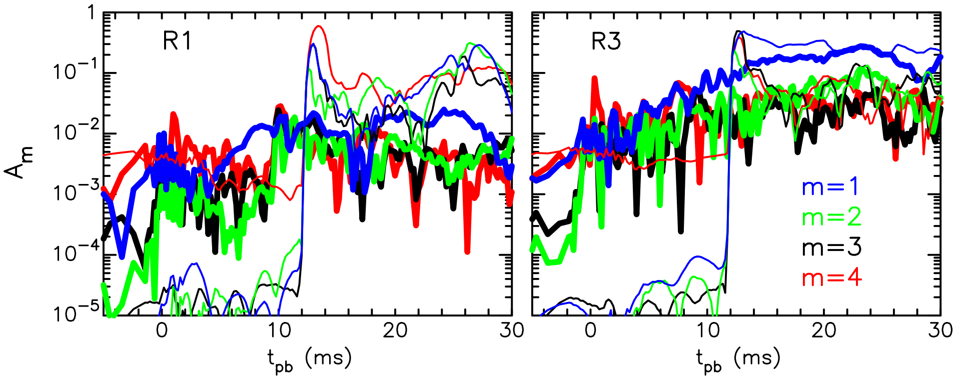

FIG. 17 (color online). Time evolution of the normalized amplitudes of the density for different azimuthal modes ($m = 1, 2, 3$, and 4) for models R1 (left) and R3 (right). Thick and thin lines are extracted at $\varpi = 20$ and 130 km, respectively.

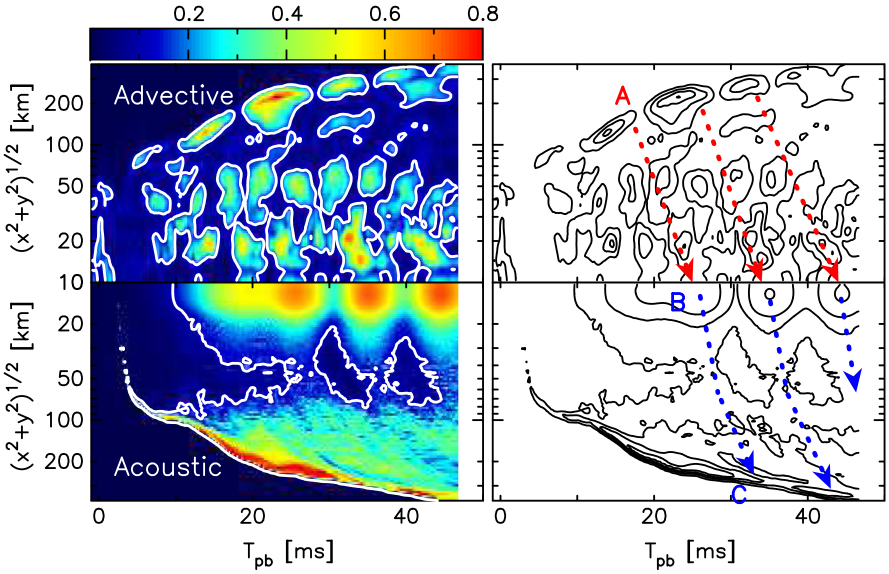

FIG. 18 (color online). (Left) Spacetime diagrams of the one-armed spiral components of vorticity (top) and acoustic waves (bottom) (see text for more details). (Right) To guide the eyes, dotted arrows are inserted to illustrate the advective-acoustic cycle on top of the contour lines from the left panels.

enough to lead to a generation of higher order nonaxisymmetric daughter modes $m \geq 2$ (see Fig. 3 in [17], and Fig. 21 in [23]). After the $m = 2$ deformation in the vicinity of the PNS, which is the most efficient GW emitter mode, a stronger GW emission with ~1 kHz frequency would be visible whose strength is also expected to overwhelm GWs emitted from outer region $R \gtrsim 60$ km. In order to see much clearer features of the low-$T/|W|$ instability, we should have continued our three-dimensional models well beyond 100 ms postbounce, i.e., until generation of higher-order nonaxisymmetric daughter modes, which is computationally expensive and is beyond the scope of this study.

Now we move on to the next discussion about one-armed spiral waves. By carefully looking at the top panels (Fig. 11), kinks are formed at the triple points where the standing shock and the spiral wave meets. Such type of morphology has been ubiquitously observed in previous simulations aiming to unravel the nature of the SASI [74,76,112–117]). To check more carefully in our results whether the advective-acoustic cycle [118,119] is running or not, we plot in Fig. 18 the spacetime diagram of vorticity (top panel, denoted by "Advective") and acoustic amplitudes (bottom panel, by "Acoustic") for model R3. Here the two quantities are evaluated as

$$\tilde{a}(\varpi) = \frac{\int_0^{2\pi} X(\varpi, \phi, z = 0) Y_{1,1}(\pi/2, \phi) d\phi}{\int_0^{2\pi} X(\varpi, \phi, z = 0) Y_{0,0}(\pi/2, \phi) d\phi}, \qquad (50)$$

where $X = \varpi \nabla \cdot (v_\phi \mathbf{e}_\phi)^{13}$ [119] and $X = p$ (p the pressure) are for the vorticity and acoustic amplitudes, respectively, $\varpi = \sqrt{x^2 + y^2}$, $\phi = \tan^{-1}(y/x)$, and $Y_{l,m}(\theta, \phi)$ are

---

[13] Here $\mathbf{e}_\phi$ is a unit azimuthal vector.

the spherical harmonics. Note that purely sloshing SASI modes were studied in detail based on two-dimensional simulations [119], but here we primarily focus on the $(l, m) = (1, 1)$ mode to extract the characteristic pattern of the one-armed spiral wave.

To guide the eyes, the right panel in Fig. 18 illustrates propagation of the advective (red lines) and acoustic waves (blue lines), respectively. Just behind the shock (see, point "A" in the top right panel), the generated vorticities go down to the PNS surface (e.g., close to the point "B"). This is supported by the arranged direction (e.g., from top-left to down-right direction in the panel) of the bumpy islands, each of which is separated by black contour lines. The reddish regions at $R \sim 10-20$ km after $T_{\rm pb} \sim 20$ ms (see the bottom left color map) represent strong generation of the acoustic waves near the PNS. They propagate outward until they hit the shock. This is seen from the direction of the greenish stripes in the color map (bottom left), which is symbolically drawn by blue lines in the bottom right panel. As indicated by red lines after point A (top right), the advective-acoustic cycle is in operation subsequently. Above features are in good agreement with [118,119] (see references therein), although the SASI signatures are not as clearly discernible as in the previous two-dimensional [120] or three-dimensional simulations [112,117] due to the short postbounce evolution in this study.

In Fig. 18, stronger acoustic waves are generated at $T_{\rm pb} \sim 27$, 35, and 44 ms near the PNS approximately in the time interval of ∼8 ms. This timescale is close to the characteristic GW frequency of the spiral waves ($F_{\rm char} = 200$–250 Hz. e.g., in Fig. 6). In order to better address the origin of $F_{\rm char} \sim 200$–250 Hz, Fig. 19 shows angle-averaged frequencies associated with the rotational velocity ($\Omega_{\rm rot}$, dotted lines) and the acoustic wave ($\Omega_{\rm rot} + \Omega_{\rm aco}$, solid lines) in the equatorial plane. Note that they are, respectively, defined as

$$\Omega_{\rm rot} \equiv 2\frac{V_\phi}{2\pi\sqrt{x^2+y^2}}, \tag{51}$$

$$\Omega_{\rm aco} \equiv 2\frac{C_s}{2\pi\sqrt{x^2+y^2}}, \tag{52}$$

and the sum ($\Omega_{\rm rot} + \Omega_{\rm aco}$) is a measure to estimate the propagation timescale of the acoustic wave on top of the rotating medium. As seen, the acoustic frequency (solid lines) shows $\Omega_{\rm aco} + \Omega_{\rm rot} \sim 200$–250 Hz in the range of 60 km $\lesssim R \lesssim$ 120 km, which is actually in good agreement with the narrow-band GW emission seen in Figs. 14 and 15. In the regions above the PNS (60 km $\lesssim R \lesssim$ 120 km), it it also shown that $\Omega_{\rm rot} \sim 100$ Hz is as high as $\Omega_{\rm aco}$. The frequency difference (∼100 Hz) between the Doppler-shifted acoustic frequency ($\Omega_{\rm rot} + \Omega_{\rm aco}$) and the purely acoustic one ($\Omega_{\rm aco}$) can naturally explain the phase shift regarding the peak GW frequency between model R3 and the remaining models with smaller initial angular momentum.

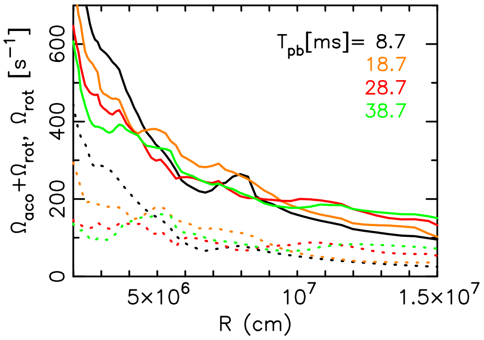

FIG. 19 (color online). Profiles of $\Omega_{\rm aco} + \Omega_{\rm rot}$ (solid lines) and $\Omega_{\rm rot}$ (dashed lines) along the equatorial direction (x axis) at different time slices (see text for more details).

Above results also show that the purely acoustic frequency $\Omega_{\rm aco} \sim 100$ Hz is less sensitive to the initial angular momentum. In fact, the GW spectra in the literature [23,33,35] generally peak at around ∼100 Hz during prompt convection. We thus speculate that significantly higher GW peaks,[14] if observed in the spectrogram during prompt convection, might be a possible signature of rapid rotation, which is unobservable if not for the GW astronomy.

F. Detectability

To discuss detectability, Fig. 20 shows the characteristic GW spectra $h_{\rm char}$ of our selected models with the design noise curves of initial LIGO [121], Advanced LIGO [6], and KAGRA [109]), assuming a source distance of 10 kpc.

For our rapidly rotating models (e.g., R2 and R3), $h_{\rm char}$ along the equatorial direction (right panel) is generally within the detection limits of the advanced detectors for an assumed distance of 10 kpc. The corresponding signal-to-noise ratio (SNR) is approximately greater than ∼10 over a wide frequency range 100 $\lesssim F \lesssim$ 1000 Hz. In accord with previous two-dimensional and three-dimensional results [17,19,38], faster initial rotation (but not too much) increase the chance for detection. The spectral peak appears at $F_{\rm peak} \sim 620$ Hz for models R3 and R2 (green and red lines in the right panel), which is associated with the maximum spike seen in the type I waveforms near bounce (e.g., Fig. 6 and the spectrogram in Fig. 12). Quantitatively this is in good agreement with Ott + 07 [17] who obtained $F_{\rm peak} \sim 600-\sim$ Hz for their counterpart three-dimensional model, in which the same Shen EOS was employed (but with much idealized microphysical treatment).

---

[14] To make it possible, a correlation analysis with neutrino signals (e.g., [38,42,121]) should be indispensable to specify the epoch of core-bounce.

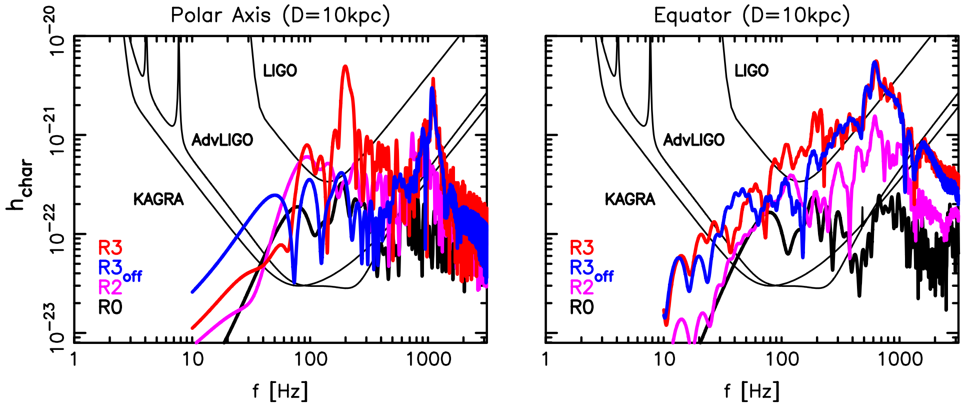

FIG. 20 (color online). Characteristic GW amplitudes h_{char} of our selected models (R3 (in red), R3$_{\mathrm{off}}$ (in blue), R2 [in magenta) and R0 (in black)] compared with the strain sensitivity of initial LIGO [121], Advanced LIGO [6], and KAGRA [109] at a source location of 10 kpc. Left and right panels are for a spectator along polar and equatorial directions, respectively. Near the bottom left corner, the initial angular velocity of each model is provided for a reference. Note that due to the small contribution from the neutrino-originated GWs, only the matter contribution is plotted here.

Seen from the polar direction, the GW spectra have two distinct peaks (e.g., green and red lines in the left panel of Fig. 20). The first peak, appearing at $F_{\mathrm{peak}} \sim 700$ Hz (model R2) and ~ 1000 Hz (model R3), is emitted during the neutronization phase ($t_{\mathrm{pb}} \lesssim 10$ ms). As mentioned earlier, this component totally vanishes in axisymmetry and it reflects the presence of precollapse density inhomogeneities. The second peaks are seen around $F_{\mathrm{peak}} \sim 100$ Hz for non- to moderately rotating models (red and black lines in the left panel). They are predominantly determined by the characteristic timescale of the acoustic waves traveling between the PNS and the stalled shock during prompt convection (see Sec. III C). Due to rapid rotation, the acoustic frequency is shifted upward $F_{\mathrm{peak}} \sim 200$ Hz in model R3 (green line in the left panel). As mentioned in the previous subsection, this is due to the Doppler effect [e.g., Eqs. (51), (52)] of the acoustic waves emitted on top of the spiral waves. The SNR of the first peak ($F_{\mathrm{peak}} = 1$ kHz) for a Galactic source is at most SNR$\sim$10 even for model R3, whose sensitivity is limited by shot noise at high frequencies. On the other hand, the SNR of the second peak achieves as high as SNR$\sim$100 (for model R3), because it is close to the maximum detector sensitivity for the advanced interferometers.

IV. SUMMARY AND DISCUSSIONS

We have studied properties of GWs from the rotating core collapse of a $15M_{\odot}$ star by performing three-dimensional full-GR hydrodynamic simulations with an approximate neutrino transport. By parametrically changing the precollapse angular momentum, we paid particular attention to the effects of rotation on the GW signatures in the early postbounce evolution. Regarding neutrino transport, we solved the energy-independent set of radiation energy and momentum based on the Thorne's momentum formalism. In addition to the matter GW signals, we took into account GWs from anisotropic neutrino emission. In addition to common GW signatures obtained in previous two-dimensional axisymmetric studies, our results showed several nonaxisymmetric features in the waveforms which can be explored only by three-dimensional simulations.

Among the common features are the type I waveforms emitted along the equatorial direction, which have comparable amplitudes with those in previous three-dimensional GR studies [17,38]. The wave amplitude reaches a few $\times 100$ cm for our most rapidly rotating model R3. For a Galactic source, this is well within the detection limits (with the SNR $\gtrsim$10) over a wide frequency range ($100 \lesssim F \lesssim 1000$ Hz) of KAGRA or Advanced LIGO. in our moderately to rapidly rotating models. The peak GW frequency ($F_{\mathrm{peak}} \sim 620$ Hz) in the GW spectra is also comparable to Ott + 07 who employed the same Shen EOS for hadronic matter. During prompt convection, the gravitational waveforms do not show any qualitative differences except for the most rapidly rotating model R3. The wave amplitude is $|A| \sim 10$ cm (non- and slowly rotating models) and $|A| \sim 20$ cm (moderately one) which are consistent with previous GR simulations [35,38] and these signals reach the SNR$\sim$8, independently of the observer direction.

We also studied neutrino luminosities, the average neutrino energies, and the waveforms associated with anisotropic neutrino emission. Rotation makes the neutrino luminosity and the average energies higher toward the polar direction, and conversely lower along the equatorial direction. These features are consequences of rotational flattening of the central core and neutrino spheres. The stronger neutrino emission toward the rotational axis leads to a quasimonotonically increasing trend in the wave amplitude, as qualitatively similar to [28] who employed more sophisticated neutrino transport. The impact of rapid rotation on the neutrino GWs was found only for the polarized wave mode A_+II in our most rapidly rotating model R3.

Our findings clearly show that nonaxisymmetric instabilities play an essential role in determining the GW signatures in the rotating postbounce evolution. By analyzing the GW spectrograms, the GW emission toward the rotational axis has two distinct features, which appears at the higher ($F \sim 700 - 1000$ Hz) and lower frequency domain ($F \sim 100 - 200$ Hz), respectively. The higher one near bounce, which appears clearly in our moderately and rapidly rotating models, comes from the conventional rotating-bounce signal. For a Galactic source, their signals achieve SNR∼5–10 for the advanced detectors. The lower one seen in non- to moderately rotating models is originated from spiral waves that develop under the control predominantly by the advective-acoustic cycle. In our most rapidly rotating model, the lower peak frequency is shifted upward to $F \sim 200$ Hz which is due to the Doppler effect [e.g., Eqs. (51), (52)] of the acoustic waves emitted on top of the spiral waves. Regarding the detectability, the relevant GW frequencies are close to the maximum detector sensitivity for the second generation interferometers (e.g., KAGRA and Advanced LIGO), which is thus expected to be detectable (SNR ∼100) for a Galactic source.

Finally we would like to discuss some of the limitations of the present work. For a more quantitative GW prediction, the simplifications in the employed neutrino reaction (and the gray transport scheme) should be improved, which we regard as the most urgent task (Kuroda *et al.*, in preparation). We need to conduct a convergence check in which a numerical gridding is changed in a parametric manner, although it is too computational expensive to do so for our three-dimensonal GR models at present. In addition, we need to run as many models as possible to study the dependencies of the precollapse density inhomogeneities, the progenitor dependence, the initial rotation rates, and magnetic fields on the GW signals. Some good news is that we have access to the "K-computer," which is among the world's fastest Peta-scale supercomputers. By utilizing it, we hope to study these important themes one by one in the near future.

ACKNOWLEDGMENTS

T. K. would like to thank continuous support from F.-K. Thielemann. T. T. and K. K. are thankful to K. Sato for continuing encouragements. K. K. acknowledges helpful discussions with Thierry Foglizzo, Christian Ott, Rodrigo Fernandez, and H. T. Janka during the INT Program INT-12-2a at the University of Washington (2012). Numerical computations were carried out in part on XT4 and the general common use computer system at the center for Computational Astrophysics, CfCA, the National Astronomical Observatory of Japan, Oakleaf FX10 at Supercomputing Division in University of Tokyo, and on SR16000 at YITP in Kyoto University. This study was supported in part by the Grants-in-Aid for Scientific Research from the Ministry of Education, Science and Culture of Japan (No. 20740150, No. 23540323, No. 23340069, and No. 24244036) and by the HPCI Strategic Program of Japanese MEXT.

[1] E. Mueller, Astron. Astrophys. **114**, 53 (1982).

[2] R. Weiss, in Sources of Gravitational Radiation: Proc. of the Batelle Seattle Workshop, edited by L. L. Smarr (Cambridge University Press, Cambridge, England, 1979), p. 7.

[3] R. Epstein, Detection of Gravitational Radiation., in Sources of Gravitational Radiation: Proc. of the Batelle Seattle Workshop, edited by L. L. Smarr (Cambridge University Press, Cambridge, England, 1979), p. 69.

[4] D. H. Douglass and V. B. Braginsky, in *General Relativity: An Einstein Centenary Survey*, edited by S. W. Hawking and W. Israel (Cambridge University Press, Cambridge, England, 1979), p. 90.

[5] J. Weber, in *General Relativity and Gravitation, Einstein commemorative volume*, edited by A. Held (Plenum, New York, 1980).

[6] G. M. Harry (LIGO Scientific Collaboration), Classical Quantum Gravity **27**, 084006 (2010).

[7] J. Degallaix *et al.*, *Advanced Virgo Status, in 9th LISA Symposium*, Astronomical Society of the Pacific Conference Series, Vol. 467, edited by G. Auger *et al.* (Astronomical Society of the Pacific, San Francisco, 2013), p. 151.

[8] K. Somiya, Classical Quantum Gravity **29**, 124007 (2012).

[9] C. D. Ott, Classical Quantum Gravity **26**, 063001 (2009).

[10] K. Kotake, C. R. Phys. **14**, 318 (2013).

[11] R. Moenchmeyer, G. Schaefer, E. Mueller, and R. E. Kates, Astron. Astrophys. **246**, 417 (1991).

[12] S. Yamada and K. Sato, Astrophys. J. **450**, 245 (1995).

[13] T. Zwerger and E. Mueller, Astron. Astrophys. **320**, 209 (1997).

[14] K. Kotake, S. Yamada, and K. Sato, Phys. Rev. D **68**, 044023 (2003).

[15] M. Shibata and Y.-I. Sekiguchi, Phys. Rev. D **69**, 084024 (2004).

[16] C. D. Ott, A. Burrows, E. Livne, and R. Walder, Astrophys. J. **600**, 834 (2004).

[17] C. D. Ott, H. Dimmelmeier, A. Marek, H.-T. Janka, I. Hawke, B. Zink, and E. Schnetter, Phys. Rev. Lett. **98**, 261101 (2007).

[18] C. D. Ott, H. Dimmelmeier, A. Marek, H.-T. Janka, B. Zink, I. Hawke, and E. Schnetter, Classical Quantum Gravity **24**, S139 (2007).

[19] H. Dimmelmeier, J. A. Font, and E. Müller, Astron. Astrophys. **393**, 523 (2002).

[20] H. Dimmelmeier, C. D. Ott, H.-T. Janka, A. Marek, and E. Müller, Phys. Rev. Lett. **98**, 251101 (2007).

[21] H. Dimmelmeier, C. D. Ott, A. Marek, and H.-T. Janka, Phys. Rev. D **78**, 064056 (2008).

[22] S. Scheidegger, T. Fischer, S. C. Whitehouse, and M. Liebendörfer, Astron. Astrophys. **490**, 231 (2008).

[23] S. Scheidegger, R. Käppeli, S. C. Whitehouse, T. Fischer, and M. Liebendörfer, Astron. Astrophys. **514**, A51 (2010).

[24] K. Kotake, S. Yamada, K. Sato, K. Sumiyoshi, H. Ono, and H. Suzuki, Phys. Rev. D **69**, 124004 (2004).

[25] A. Burrows and J. Hayes, Phys. Rev. Lett. **76**, 352 (1996).

[26] E. Mueller and H.-T. Janka, Astron. Astrophys. **317**, 140 (1997).

[27] C. L. Fryer, Astrophys. J. Lett. **601**, L175 (2004).

[28] E. Müller, M. Rampp, R. Buras, H.-T. Janka, and D. H. Shoemaker, Astrophys. J. **603**, 221 (2004).

[29] A. Marek, H.-T. Janka, and E. Müller, Astron. Astrophys. **496**, 475 (2009).

[30] K. Kotake, N. Ohnishi, and S. Yamada, Astrophys. J. **655**, 406 (2007).

[31] K. Kotake, W. Iwakami, N. Ohnishi, and S. Yamada, Astrophys. J. Lett. **697**, L133 (2009).

[32] K. Kotake, W. Iwakami, N. Ohnishi, and S. Yamada, Astrophys. J. **704**, 951 (2009).

[33] J. W. Murphy, C. D. Ott, and A. Burrows, Astrophys. J. **707**, 1173 (2009).

[34] E. Müller, H.-T. Janka, and A. Wongwathanarat, Astron. Astrophys. **537**, A63 (2012).

[35] B. Müller, H.-T. Janka, and A. Marek, Astrophys. J. **766**, 43 (2013).

[36] K. Kotake, W. Iwakami-Nakano, and N. Ohnishi, Astrophys. J. **736**, 124 (2011).

[37] É. É. Flanagan and S. A. Hughes, Phys. Rev. D **57**, 4566 (1998).

[38] C. D. Ott, E. Abdikamalov, E. O'Connor, C. Reisswig, R. Haas, P. Kalmus, S. Drasco, A. Burrows, and E. Schnetter, Phys. Rev. D **86**, 024026 (2012).

[39] A. Mezzacappa, Annu. Rev. Nucl. Part. Sci. **55**, 467 (2005).

[40] H.-T. Janka, Annu. Rev. Nucl. Part. Sci. **62**, 407 (2012).

[41] K. Kotake *et al.*, arXiv:1205.6284.

[42] K. Kotake *et al.*, arXiv:1204.2330.

[43] S. E. Woosley and J. S. Bloom, Annu Rev Astron Astrophys **44**, 507 (2006).

[44] G. S. Bisnovatyi-Kogan, I. P. Popov, and A. A. Samokhin, Astrophys. Space Sci. **41**, 287 (1976).

[45] J. M. LeBlanc and J. R. Wilson, Astrophys. J. **161**, 541 (1970).

[46] K. Kotake, K. Sato, and K. Takahashi, Rep. Prog. Phys. **69**, 971 (2006).

[47] A. Burrows, L. Dessart, E. Livne, C. D. Ott, and J. Murphy, Astrophys. J. **664**, 416 (2007).

[48] T. Takiwaki, K. Kotake, and K. Sato, Astrophys. J. **691**, 1360 (2009).

[49] T. Takiwaki and K. Kotake, Astrophys. J. **743**, 30 (2011).

[50] S. A. Balbus and J. F. Hawley, Rev. Mod. Phys. **70**, 1 (1998).

[51] M. Obergaulinger, P. Cerdá-Durán, E. Müller, and M. A. Aloy, Astron. Astrophys. **498**, 241 (2009).

[52] Y. Masada, T. Takiwaki, K. Kotake, and T. Sano, Astrophys. J. **759**, 110 (2012).

[53] B. D. Metzger, D. Giannios, T. A. Thompson, N. Bucciantini, and E. Quataert, Mon. Not. R. Astron. Soc. **413**, 2031 (2011).

[54] A. I. MacFadyen, S. E. Woosley, and A. Heger, Astrophys. J. **550**, 410 (2001).

[55] S. Harikae, T. Takiwaki, and K. Kotake, Astrophys. J. **704**, 354 (2009).

[56] S. Harikae, K. Kotake, and T. Takiwaki, Astrophys. J. **713**, 304 (2010).

[57] P. Mészáros, Rep. Prog. Phys. **69**, 2259 (2006).

[58] M. Shibata, Y. T. Liu, S. L. Shapiro, and B. C. Stephens, Phys. Rev. D **74**, 104026 (2006).

[59] M. Obergaulinger, M. A. Aloy, and E. Müller, Astron. Astrophys. **450**, 1107 (2006).

[60] S. Kawamura *et al.*, Classical Quantum Gravity **23**, S125 (2006).

[61] N. Andersson, Classical Quantum Gravity **20**, R105 (2003).

[62] C. L. Fryer and K. C. B. New, Living Rev. Relativity **14**, 1 (2011).

[63] M. Rampp, E. Mueller, and M. Ruffert, Astron. Astrophys. **332**, 969 (1998).

[64] M. Shibata, K. Taniguchi, and K. Uryū, Phys. Rev. D **71**, 084021 (2005).

[65] J. M. Centrella, K. C. B. New, L. L. Lowe, and J. D. Brown, Astrophys. J. Lett. **550**, L193 (2001).

[66] M. Saijo, T. W. Baumgarte, and S. L. Shapiro, Astrophys. J. **595**, 352 (2003).

[67] A. L. Watts, N. Andersson, and D. I. Jones, Astrophys. J. Lett. **618**, L37 (2005).

[68] S. Ou and J. E. Tohline, Astrophys. J. **651**, 1068 (2006).

[69] P. Cerdá-Durán, V. Quilis, and J. A. Font, Comput. Phys. Commun. **177**, 288 (2007).

[70] C. D. Ott, S. Ou, J. E. Tohline, and A. Burrows, Astrophys. J. Lett. **625**, L119 (2005).

[71] M. Liebendörfer, Astrophys. J. **633**, 1042 (2005).

[72] M. Saijo and S. Yoshida, Mon. Not. R. Astron. Soc. **368**, 1429 (2006).

[73] J. C. B. Papaloizou and J. E. Pringle, Mon. Not. R. Astron. Soc. **213**, 799 (1985).

[74] J. M. Blondin and A. Mezzacappa, Nature (London) **445**, 58 (2007).

[75] W. Iwakami, K. Kotake, N. Ohnishi, S. Yamada, and K. Sawada, Astrophys. J. **678**, 1207 (2008).

[76] T. Yamasaki and T. Foglizzo, Astrophys. J. **679**, 607 (2008).

[77] A. Wongwathanarat, N. J. Hammer, and E. Müller, Astron. Astrophys. **514**, A48 (2010).

[78] F. Hanke, B. Mueller, A. Wongwathanarat, A. Marek, and H.-T. Janka, arXiv:1303.6269.

[79] W. Keil, H.-T. Janka, and E. Mueller, Astrophys. J. Lett. **473**, L111 (1996).

[80] S. W. Bruenn and T. Dineva, Astrophys. J. Lett. **458**, L71 (1996).
[81] L. Dessart, A. Burrows, E. Livne, and C. D. Ott, Astrophys. J. **645**, 534 (2006).
[82] R. Buras, M. Rampp, H.-T. Janka, and K. Kifonidis, Astron. Astrophys. **447**, 1049 (2006).
[83] T. Kuroda, K. Kotake, and T. Takiwaki, Astrophys. J. **755**, 11 (2012).
[84] B. Müller, H. Dimmelmeier, and E. Müller, Astron. Astrophys. **489**, 301 (2008).
[85] C. D. Ott *et al.*, arXiv:1210.6674.
[86] T. Kuroda and H. Umeda, Astrophys. J. Suppl. Ser. **191**, 439 (2010).
[87] M. Shibata and T. Nakamura, Phys. Rev. D **52**, 5428 (1995).
[88] T. W. Baumgarte and S. L. Shapiro, Phys. Rev. D **59**, 024007 (1999).
[89] C. D. Levermore, J. Quant. Spectrosc. Radiat. Transfer **31**, 149 (1984).
[90] M. Shibata, K. Kiuchi, Y. Sekiguchi, and Y. Suwa, Prog. Theor. Phys. **125**, 1255 (2011).
[91] S. E. Woosley and T. A. Weaver, Astrophys. J. Suppl. Ser. **101**, 181 (1995).
[92] M. Alcubierre and B. Brügmann, Phys. Rev. D **63**, 104006 (2001).
[93] K. S. Thorne, Mon. Not. R. Astron. Soc. **194**, 439 (1981).
[94] H. Shen, H. Toki, K. Oyamatsu, and K. Sumiyoshi, Nucl. Phys. A **637**, 435 (1998).
[95] A. Heger, S. E. Woosley, and H. C. Spruit, Astrophys. J. **626**, 350 (2005).
[96] A. Heger and N. Langer, Astrophys. J. **544**, 1016 (2000).
[97] H. Spruit and E. S. Phinney, Nature (London) **393**, 139 (1998).
[98] C. Reisswig, C. D. Ott, U. Sperhake, and E. Schnetter, Phys. Rev. D **83**, 064008 (2011).
[99] Y. Sekiguchi, Prog. Theor. Phys. **124**, 331 (2010).
[100] C. W. Misner, K. S. Thorne, and J. A. Wheeler, *Gravitation*, Physics Series (W. H. Freeman, San Francisco, 1973).
[101] L. S. Finn and C. R. Evans, Astrophys. J. **351**, 588 (1990).
[102] K.-i. Oohara, T. Nakamura, and M. Shibata, Prog. Theor. Phys. Suppl. **128**, 183 (1997).
[103] K. Kiuchi, M. Shibata, and S. Yoshida, Phys. Rev. D **78**, 024029 (2008).
[104] S. E. Woosley and A. Heger, Phys. Rep. **442**, 269 (2007).
[105] H.-T. Janka and R. Moenchmeyer, Astron. Astrophys. **226**, 69 (1989).
[106] K. Kotake, S. Yamada, and K. Sato, Astrophys. J. **595**, 304 (2003).
[107] C. D. Ott, A. Burrows, L. Dessart, and E. Livne, Astrophys. J. **685**, 1069 (2008).
[108] V. B. Braginskii and K. S. Thorne, Nature (London) **327**, 123 (1987).
[109] K. Kuroda and LCGT Collaboration, Classical Quantum Gravity **27**, 084004 (2010).
[110] T. Foglizzo, P. Galletti, L. Scheck, and H.-T. Janka, Astrophys. J. **654**, 1006 (2007).
[111] T. Foglizzo, Astrophys. J. **694**, 820 (2009).
[112] R. Fernández, Astrophys. J. **725**, 1563 (2010).
[113] J. M. Blondin, A. Mezzacappa, and C. DeMarino, Astrophys. J. **584**, 971 (2003).
[114] L. Scheck, T. Plewa, H.-T. Janka, K. Kifonidis, and E. Müller, Phys. Rev. Lett. **92**, 011103 (2004).
[115] N. Ohnishi, K. Kotake, and S. Yamada, Astrophys. J. **641**, 1018 (2006).
[116] T. Foglizzo, L. Scheck, and H.-T. Janka, Astrophys. J. **652**, 1436 (2006).
[117] W. Iwakami, K. Kotake, N. Ohnishi, S. Yamada, and K. Sawada, Astrophys. J. **700**, 232 (2009).
[118] T. Foglizzo and M. Tagger, Astron. Astrophys. **363**, 174 (2000).
[119] L. Scheck, H.-T. Janka, T. Foglizzo, and K. Kifonidis, Astron. Astrophys. **477**, 931 (2008).
[120] B. Müller, H.-T. Janka, and A. Heger, Astrophys. J. **761**, 72 (2012).
[121] F. Halzen and G. G. Raffelt, Phys. Rev. D **80**, 087301 (2009).